Chapter 5
Ion Thruster Accelerator Grids

Ion thrusters are characterized by the electrostatic acceleration of ions extracted from the plasma generator [1]. An illustration of a direct current (DC) electron bombardment ion thruster showing the ion accelerator, the plasma generator, and the neutralizer cathode was shown in Fig. 1-1. The ion accelerator consists of electrically biased multi-aperture grids, and this assembly is often called the *ion optics*. The design of the grids is critical to the ion thruster operation and is a trade between performance, life, and size. Since ion thrusters need to operate for years in most applications, life is often a major design driver. However, performance and size are always important in order to satisfy the mission requirements for thrust and specific impulse (Isp) and to provide a thruster size and shape that fits onto the spacecraft.

There are many factors that determine the grid design in ion thrusters. The grids must extract the ions from the discharge plasma and focus them through the downstream accelerator grid (accel grid) and decelerator grid (decel grid) (if used). This focusing has to be accomplished over the range of ion densities produced by the discharge chamber plasma profile that is in contact with the screen grid, and also over the throttle range of different power levels that the thruster must provide for the mission. Since the screen grid transparency was shown in Chapter 4 to directly impact the discharge loss, the grids must minimize ion impingement on the screen grid and extract the maximum number of the ions that are delivered by the plasma discharge to the screen grid surface. In addition, the grids must minimize neutral atom loss out of the discharge chamber to maximize the mass utilization efficiency of the thruster. High ion transparency and low neutral transparency drives the grid design toward larger screen grid holes and smaller accel grid holes, which impacts the optical focusing of the ions and the beam divergence. The beam divergence also should be minimized to reduce thrust loss and plume impact on the spacecraft or solar arrays, although some amount of beam divergence can usually be

accommodated. Finally, grid life is of critical importance and often drives thruster designers to compromises in performance or alternative grid materials. In this chapter, the factors that determine grid design and the principles of the ion accelerators used in ion thrusters will be described.

5.1 Grid Configurations

To accelerate ions, a potential difference must be established between the plasma produced inside the thruster plasma generator and the ambient space plasma. As shown in Chapter 3, simply biasing the anode of a DC plasma generator or the electrodes of a radio frequency (rf) plasma generator relative to a spacecraft or plasma in contact with the space potential does not result in ion beam generation because the voltage will just appear in the sheath at the plasma boundary with the walls. If the potential is small compared to the electron temperature T_e, then a Debye sheath is established, and if the potential is very large compared to T_e, then a Child–Langmuir sheath exists. Therefore, to accelerate ions to high energy, it is necessary to reduce the dimension of an aperture at the plasma boundary to the order of the Child–Langmuir distance to establish a sheath that will accelerate the ions with reasonable directionality (good focusing) and reflect the electrons from the plasma. Figure 5-1 shows the Child–Langmuir length calculated from Eq. (3.7-34) for two singly charged ion current densities at an acceleration voltage of 1500 V. For xenon, the characteristic aperture dimension at this voltage is on the order of 2 to 5 mm and will decrease if the applied voltage is reduced or the current in the aperture is increased.
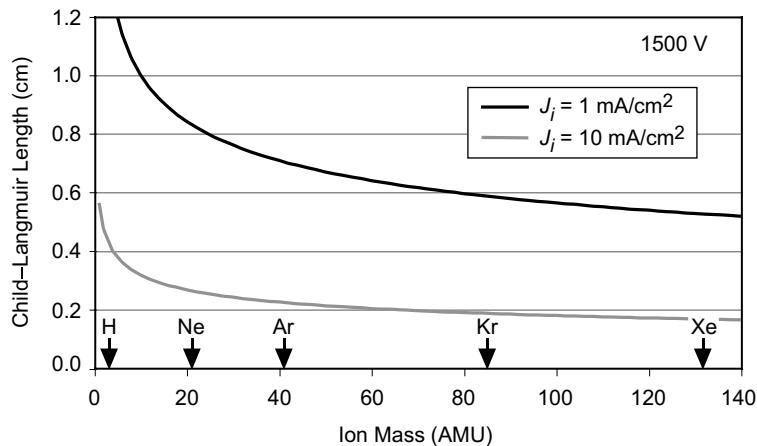

Fig. 5-1. Child–Langmuir sheath length versus ion mass for two ion current densities at 1500-V acceleration voltage.

The ion current obtainable from each grid aperture is then limited by space charge. For a 0.25-cm-diameter aperture extracting the space-charge-limited xenon current density of about 5 mA/cm^2 at 1500 V [from Eq. (3.7-56)], the total ion current per aperture is only 0.25 mA. Assuming this produces a well-focused beamlet, the thrust produced by this current and voltage according to Eq. (2.3-9) is only about 16 μnewtons. Therefore, multiple apertures must be used to obtain higher beam currents from the ion engine to increase the thrust. For example, to extract a total of 1 A of xenon ion current for this case would require over 4000 apertures, which would produce over 60 mN of thrust. In reality, for reliable high-voltage operation, and due to non-uniformities in the plasma generator producing varying ion current densities to the boundary, the current density is usually chosen to be less than the Child–Langmuir space charge maximum, and an even larger number of apertures are required. This ultimately determines the size of the ion thruster.

Figure 5-2 shows a simplified one-dimensional (1-D) view of one of these biased apertures facing the thruster plasma. The Child–Langmuir sheath is established by the bias potential between the thruster plasma and the accelerator grid and is affected by the current density of the xenon ions arriving at the sheath edge from the Bohm current. Ions that arrive on axis with the aperture are accelerated through to form the beam. However, ions that miss the aperture are accelerated into the accel grid and can erode it rapidly. For this reason, a "screen" grid with apertures aligned with the accel grid is placed upstream of the accel grid to block these ions. This is the classic two-grid accelerator system [1,2]. The screen grid is normally either allowed to float electrically or is biased to the cathode potential of the plasma generator to provide some confinement of the electrons in the plasma and so that ions that strike it have a relatively low energy and cause little sputtering. In practice, the grids are made of refractory metals or carbon-based materials, and the apertures are close-packed in a
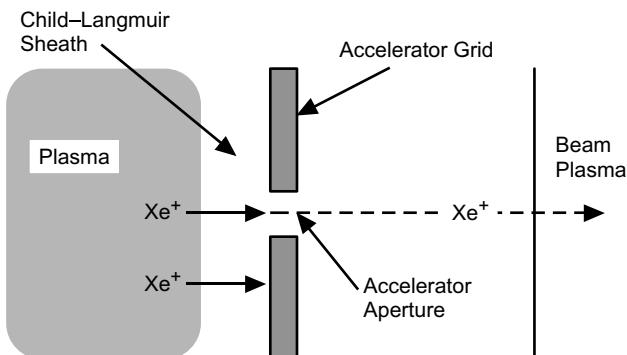

Fig. 5-2. Simplified 1-D view of an accelerator aperture in contact with a plasma.

hexagonal structure to produce a high transparency to the ions from the plasma generator. These grids are also normally dished to provide structural rigidity to survive launch loads and to ensure that they expand uniformly together during thermal loading [1,3].

The electrical configuration of an ion thruster accelerator is shown schematically in Fig. 5-3. The high-voltage bias supply (called the screen supply) is normally connected between the anode and the common of the system, which is usually connected to the neutralizer cathode (called "neutralizer common") that provides electrons to neutralize the beam. Positive ions born in the discharge chamber at high positive voltage are then accelerated out of the thruster. The accel grid is biased negative relative to the neutralizer common to prevent the very mobile electrons in the beam plasma from back-streaming into the thruster, which produces localized heating in the discharge chamber by energetic electron bombardment, and ultimately overloads the
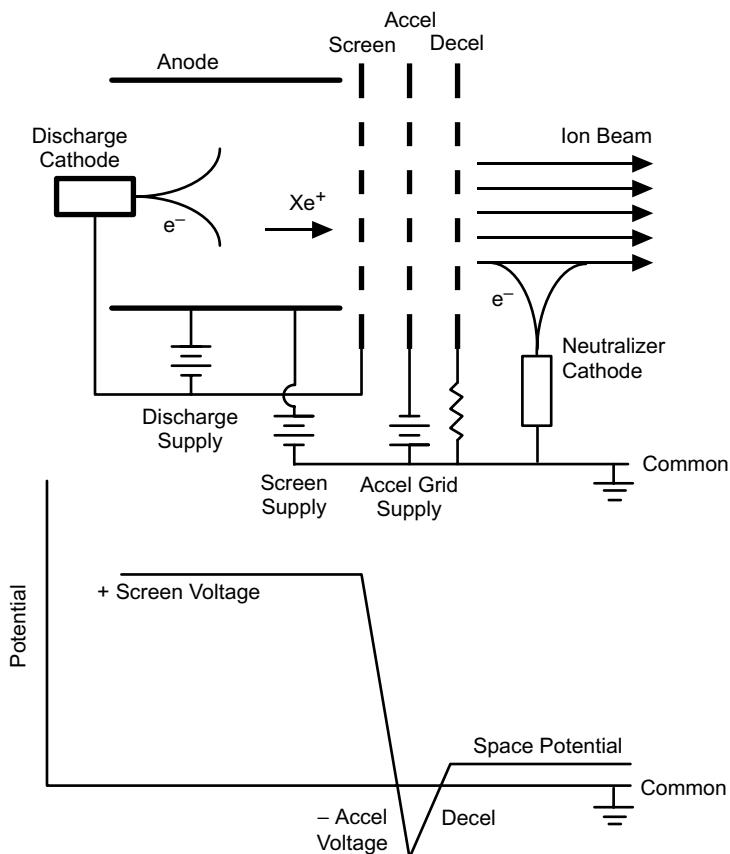

Fig. 5-3. Electrical schematic of a DC discharge ion thruster without the cathode heater and keeper supplies.

screen supply if the backstreaming current becomes large. The ion beam is current neutralized and quasi-neutral (nearly equal ion and electron densities) by the electrons extracted from the neutralizer cathode. Fortunately, the thruster self-biases the neutralizer common potential sufficiently negative relative to the beam potential to produce the required number of electrons to current neutralize the beam.

Figure 5-3 showed a generic thruster that includes a three-grid accelerator system, where a final grid called the "decel grid" is placed downstream of the accel grid. This grid shields the accel grid from ion bombardment by charge-exchanged ions produced in the beam backflowing toward the thruster, and eliminates the downstream "pits-and-grooves erosion" that will be discussed in Section 5.6. Three-grid systems then potentially have longer accel grid life than two grid systems and generate less sputtered material into the plume that can deposit on the spacecraft. These benefits are offset by the increased complexity of including the third grid.

In actual design, the diameter of each accel grid aperture is minimized to retain unionized neutral gas in the plasma generator, and the screen grid transparency is maximized so that that the grids extract the maximum possible number of ions from the plasma. The electrode diameters and spacing are then optimized to eliminate direct interception of the beam ions on the accel grid, which would cause rapid erosion due to the high ion energy. A schematic example of a three-grid system showing the ion trajectories calculated by a two-dimensional (2-D) ion optics code [4] is shown in Fig. 5-4. The ions are focused sufficiently by this electrode design to pass through the accel grid without direct interception. On the downstream side of the accel grid, the negative accel-grid bias applied to avoid electron backstreaming results in a relatively small deceleration of the ions before they enter the quasi-neutral beam potential region. This high transparency, strong "accel–decel" geometry typical of ion thrusters results in some beamlet divergence, as suggested by the figure. However, this small beamlet angular divergence of typically a few degrees causes negligible thrust lost because the loss scales as $\cos\theta$, and because most of the beam divergence discussed in Chapter 2 related to the thrust correction factor is due to the dishing of the grids.

The amount of current that an ion accelerator can extract and focus into a beam for a given applied voltage is related to the space-charge effects characterized by the Child–Langmuir equation and is called the perveance:

$$P \equiv \frac{I_b}{V^{3/2}}.$$

(5.1-1)

The maximum perveance that can be achieved by an accelerator is given by the coefficient in the Child–Langmuir equation:

$$P_{\max} \equiv \frac{4\varepsilon_o}{9}\sqrt{\frac{2q}{M}}\left[A/V^{3/2}\right]. \qquad (5.1\text{-}2)$$

For an electron accelerator, this coefficient is the familiar value of 2.33×10^{-6} $A/V^{3/2}$, and for singly charged xenon ions it is 4.8×10^{-9} $A/V^{3/2}$. For round apertures, the Child–Langmuir equation can be written

$$J = \frac{I_b}{\left(\pi D^2 \big/ 4\right)} = \frac{4\varepsilon_o}{9}\sqrt{\frac{2q}{M}}\frac{V^{3/2}}{d^2}\left[A/m^2\right], \qquad (5.1\text{-}3)$$

where d is the effective grid gap and D is the beamlet diameter. Inserting Eq. (5.1-3) into Eq. (5.1-1), the maximum perveance for round apertures is

$$P_{\max} \equiv \frac{\pi\varepsilon_o}{9}\sqrt{\frac{2q}{M}}\left(\frac{D^2}{d^2}\right)\left[A/V^{3/2}\right]. \qquad (5.1\text{-}4)$$

Therefore, to maximize the perveance of the accelerator, it is desirable to make the grid gap smaller than the aperture diameters, as illustrated in the example configuration shown in Fig. 5-4.

The ion trajectories plotted in Fig. 5-4 that do not intercept either of the grids, and the minimal beamlet divergence, result from operating at or near the optimal ion current density and voltage for the grid geometry shown. Operating at significantly less than the optimal perveance, called "under-perveance" and
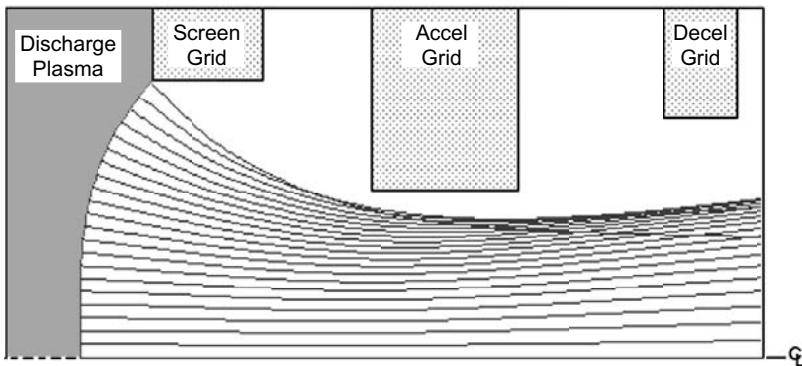

Fig. 5-4. Ion trajectories from a plasma sheath (on the left) in a half-beamlet inside an example three-grid accelerator.

corresponding to higher voltages or lower beamlet currents than the optimal combination, increases the Child–Langmuir (CL) length and pushes the sheath to the left farther into the plasma. In the extreme case, this situation can launch ions at a very large angle from the edge region near the screen aperture and cause "cross-over" trajectories, which can then produce excessive erosion of the accel grid by direct ion impingement. Likewise, operating at higher than the optimal perveance, corresponding to higher beamlet currents or lower voltages than optimal, reduces the Child–Langmuir sheath thickness, and the plasma boundary pushes toward the screen aperture. This "over-perveance" condition flattens the sheath edge and accelerates ions directly into the accel grid, again causing excessive erosion. The optical performance and life of any grid design, therefore, is acceptable only over a limited range in voltage and current density, which will be discussed in Section 5.3. For this reason, the uniformity of the plasma over the grid area is important to avoid either cross-over or direct interception in different regions of the ion optics that strongly degrade the life of the grids.

In the two- or three-grid configurations, the geometry of the grid apertures and gaps is intended to eliminate or at least minimize direct impingement by beam ions on the most negative potential electrode in the system, namely, the accel grid. This is required to minimize sputtering of the grid by the high-energy beam ions. The screen grid does receive ion bombardment from the discharge plasma due to its finite transparency, but the ions arrive with only an energy of the order of the discharge voltage in DC discharge thrusters or the floating potential in rf or microwave thrusters. Sputter erosion of the screen grid then becomes an issue only at high discharge voltages or due to the production of high-energy ions in the hollow cathode region [5,6] that can bombard the screen grid. Likewise, the decel grid is biased near the beam plasma potential and backflowing ions produced in the beam by charge exchange impact with very low energy, which causes little or no sputtering. For two grid systems, the backflowing ions bombard the accel grid with essentially the grid bias voltage. This can cause significant sputtering of the downstream face of the accel grid and may determine the grid life.

The decelerating field produced downstream of the accelerator grid by the accel grid bias acts as a weak defocusing lens for the ions, but keeps electrons emitted by the neutralizer from entering the high field region and backstreaming at high energy into the discharge chamber. This decelerating field is set up either by applying a potential between the accelerator grid and the decel grid or by applying the bias between the accelerator grid and the hollow cathode neutralizer and allowing the low energy plasma downstream of the accelerator grid to act as a virtual anode. Unfortunately, ions generated between the grids by either charge exchange with unionized neutral gas escaping the

plasma generator or by ionization from the most energetic backstreaming electrons do strike the accel grid and erode it. Charge exchange ion erosion of the accel grid ultimately limits the grid life, which will be discussed in Section 5.6.

5.2 Ion Accelerator Basics

The thruster ion optics assembly serves three main purposes:

1) Extract ions from the discharge chamber

2) Accelerate ions to generate thrust

3) Prevent electron backstreaming

The ideal grid assembly would extract and accelerate all the ions that approach the grids from the plasma while blocking the neutral gas outflow, accelerate beams with long life and with high current densities, and produce ion trajectories that are parallel to the thruster axis with no divergence under various thermal conditions associated with changing power levels in the thruster. In reality, grids are non-ideal in each of these areas. Grids have finite transparency; thus, some of the discharge chamber ions hit the upstream "screen grid" and are not available to become part of the beam. The screen grid transparency, T_s, is the ratio of the beam current, I_b, to the total ion current, I_i, from the discharge chamber that approaches the screen grid:

$$T_s = \frac{I_b}{I_i}.$$

(5.2-1)

This ratio is determined by comparing the ion beam current with the screen grid current. The transparency depends on the plasma parameters in the discharge chamber because the hemispherical sheath edge is normally pushed slightly into the plasma by the applied voltage if the screen grid is relatively thin. The pre-sheath fields in the plasma edge then tend to steer some ions that would have gone to the screen grid into the beam. For this reason, the effective transparency of the screen grid typically exceeds the optical transparency for relatively large apertures and thin grid thicknesses. In addition, the screen grid current must be measured with the screen grid biased negative relative to cathode potential to reflect energetic electrons in the tail of the Maxwellian distribution in the plasma. The goal for screen grid design is to maximize the grid transparency to ions by minimizing the screen thickness and the webbing between screen grid holes to that required for structural rigidity.

The maximum beam current density is limited by the ion space charge in the gap between the screen and accelerator grids [2], which was discussed above

with respect to the perveance that was specified by the Child–Langmuir equation in which the sheath was considered essentially planar. The problem is that the sheath shape in the screen aperture is not planar, as seen in Fig. 5-4, and the exact shape and subsequent ion trajectories have to be solved by 2-D axi-symmetric codes. However, a modified sheath thickness can be used in the Child–Langmuir equation to approximately account for this effect, which is written as

$$J_{\max} = \frac{4\varepsilon_o}{9} \sqrt{\frac{2e}{M}} \frac{V_T^{3/2}}{\ell_e^2},$$

(5.2-2)

where V_T is the total voltage across the sheath between the two grids and the sheath thickness, , ℓ_e is given by

$$\ell_e = \sqrt{\left(\ell_g + t_s\right)^2 + \frac{d_s^2}{4}} .$$

(5.2-3)

The grid dimensions in Eq. (5.2-3) are defined in Fig. 5-5. As illustrated in the figure, the sheath is allowed to expand essentially spherically through the screen grid aperture. The sheath thickness ℓ_e accounts for this non-planar condition and has been found to be useful in predicting the space-charge-limited current in ion thruster grid configurations [1,7]. Note that the value of ℓ_g is the "hot grid gap" that occurs once the grids have expanded into their final shape during operation at a given beam current and voltage. For xenon ions,
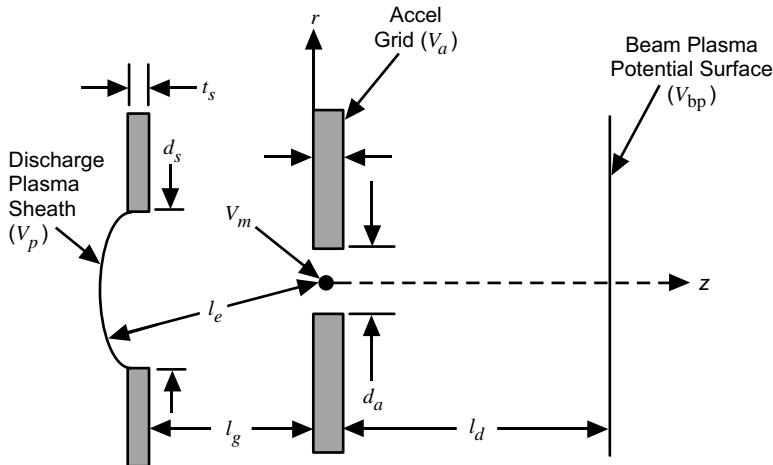

Fig. 5-5. Non-planar sheath model approximation for a two-grid system.

$$J_{max} = 4.75 \times 10^{-9} \frac{V_T^{3/2}}{\ell_e^2}. \qquad (5.2\text{-}4)$$

The units of the current density in the Child–Langmuir equations are amperes divided by the dimension used for the sheath thickness, ℓ_e, squared.

The maximum thrust per unit area possible from an ion thruster can also be found. Thrust was defined in Chapter 2 for electric thrusters as

$$T = \frac{d(mv)}{dt} = \gamma \dot{m}_i v_i. \qquad (5.2\text{-}5)$$

Assuming the ions start at rest, the ion velocity leaving the accelerator is

$$v_i = \sqrt{\frac{2eV_b}{M}}, \qquad (5.2\text{-}6)$$

where eV_b is the net beam energy. Using Eq. (2.2-3) for the time rate of change of the mass, the thrust per unit area of the grids becomes

$$\frac{T}{A_g} = \frac{J_{max}\, \gamma\, T_s M v_i}{e}, \qquad (5.2\text{-}7)$$

where A_g is the active grid area (with extraction apertures) and T_s is the grid transparency defined in Eq. (5.2-1). The effective electric field in the acceleration gap is

$$E = \frac{V_T}{\ell_e}, \qquad (5.2\text{-}8)$$

where V_T is the total voltage across the accelerator gap (the sum of the screen and accel voltages):

$$V_T = V_s + |V_a| = \frac{V_b}{R}, \qquad (5.2\text{-}9)$$

and R is the ratio of the net beam voltage to the total voltage. Using Eq. (5.2-2) for the space-charge-limited current density and the electric field from Eq. (5.2-8), the maximum achievable thrust density is

$$\frac{T_{\max}}{A_g} = \frac{4}{9} \frac{\varepsilon_o \gamma T_s}{e} \sqrt{\frac{2e}{M}} \frac{V_T^{3/2}}{\ell_e^2} M \sqrt{\frac{2eV_b}{M}} = \frac{8}{9} \varepsilon_o \gamma T_s \sqrt{R} E^2 . \qquad (5.2\text{-}10)$$

The maximum thrust density from an ion thruster increases with the screen grid transparency and the square of the electric field [8]. Ion thrusters with thin, high transparency grids operating near the perveance limit and at the maximum possible electric field in the acceleration gap will produce the most thrust for a given grid area. A key feature of ion thrusters illustrated by Eq. (5.2-10) is that the thrust density is independent of propellant mass.

The net-to-total voltage ratio from Eq. (5.2-9) is given by

$$R = \frac{V_b}{V_T} = \frac{V_b}{V_s + |V_a|} . \qquad (5.2\text{-}11)$$

This equation describes the relative magnitude of the accel grid bias relative to the screen potential. Operating with small values of R increases the total voltage between the screen and accel grids, which, from Eq. (5.2-2), results in a higher current density of ions accelerated from the thruster. While it appears desirable to operate with very small values of R (large accel grid negative bias) to increase the current capability of a grid set, this results in higher energy ion bombardment of the accel grid and shortens grid life. Operating with small values of R will also change the beam divergence, but this is a relatively small effect in ion thrusters for most grid designs. For applications where thruster life is important, the magnitude of accel grid bias voltage is usually minimized to the value required to just avoid electron backstreaming, and the value of R typically ranges from 0.8 to 0.9. Finally, Eq. (5.2-10) suggests that the thrust density depends on the square root of R and would increase slowly with higher beam-to-total voltage ratios. This is misleading because the total voltage also appears in the electric field term $(E = V_T / \ell_e)$, and so higher thrust densities actually occur with more negative accel grid bias because of the higher voltage applied across the screen-to-accel gap for a given net (beam) voltage.

Aside from mechanical tolerances, the minimum "hot-gap" grid separation, ℓ_g, is limited by the vacuum breakdown field of the grid material:

$$E = \frac{V}{\ell_g} < E_{\text{breakdown}} . \qquad (5.2\text{-}12)$$

In practice, grid breakdowns initiated by arcing or small micro-discharges between the grids cause "recycles" in which the voltages are temporarily

removed to extinguish the arc and then reapplied. It is common to also decrease the discharge plasma density during a recycle so that the reapplication of the acceleration voltages corresponds with ramping up the discharge current such that the accelerator approximately tracks the right perveance during start up. This minimizes ion bombardment of the accel grid during a recycle. To obtain reliable operation and avoid frequent recycles, the maximum field strength in the ion thruster typically is set to less than half the vacuum breakdown field. For example, if the grid spacing were a millimeter and the acceleration potential between the grids a thousand volts, the theoretical maximum xenon ion beam current density would be 15 mA/cm^2. A 25-cm-diameter, uniform-profile beam with a 75% transparent grid system would then produce about 5.5 A of beam current. In practice, because of high voltage breakdown considerations, the maximum beam current obtainable from grid sets is typically about half the theoretical maximum.

The ion thruster size is determined by the perveance limit on the beam current density and practical considerations on the grids, such as maximum grid transparency and electric field [1]. For this reason, ion thruster beam current densities are typically on the order of a tenth that found in Hall thrusters, resulting in a larger thruster footprint on the spacecraft. Alternatively, the maximum Isp that is achievable is limited by the voltage that can be applied to the grids to extract a given current density before electrical breakdown or electron backstreaming occurs [9]. Very high Isp thrusters (>10,000 s), with a size that depends on the thrust requirement, have been built and successfully tested.

5.3 Ion Optics

While the simple formulas above provide estimates of the ion accelerator optics performance, a number of computer simulation codes have been developed [4,10–17] to more accurately evaluate the ion trajectories produced by thruster grids. Ion optics codes solve in two or three dimensions the combined ion charge density and Poisson's equations for the given grid geometry and beamlet parameters [18]. These codes have been used for the design and analysis of two- and three-grid systems, and were extended to four-grid systems [19] to examine "two-stage" ion optics performance [20] for very high voltage, high Isp applications.

5.3.1   Ion Trajectories

There are a number of codes that calculate ion trajectories and grid performance in ion thrusters, and an extensive analysis of ion optics behavior in thrusters was recently completed by Farnell [21]. An example of a multi-dimensional code CEX-2D, which is an ion optics code developed at JPL that calculates ion

trajectories and charge exchange reactions between beam ions and un-ionized propellant gas in two [4] and three [17] dimensions. The CEX-2D code solves Poisson's equation, given in Eq. (3.7-8) in Chapter 3, on a regular mesh in cylindrical geometry. The code models a single set of screen and accel grid holes and assumes cylindrical symmetry. The computational space is divided into a grid of rectangular cells with up to 400 increments radially and 600 axially. The radial grid spacing is uniform; the axial spacing is allowed to increase in the downstream direction. The computational region is typically a few millimeters radially and up to 5 centimeters along the axis downstream of the final grid. With a few exceptions, the code uses a combination of algorithms used in earlier optics codes for ion thrusters [11–15].

Upstream of the accelerator grid, the electron density is obtained analytically from the barometric law assuming a Maxwellian distribution:

$$n_e(V) = n_e(0) \, \exp\left(\frac{\phi - \phi_o}{T_e} \right).$$
(5.3-1)

The upstream reference electron density, $n_e(0)$, is set equal to the input discharge chamber ion density. Downstream of the accelerator grid, the electron population is also assumed to be a Maxwellian distribution with a different reference potential:

$$n_e(V) = n_e(\infty) \, \exp\left(\frac{\phi - \phi_\infty}{T_e} \right),$$
(5.3-2)

where the downstream reference electron density, $n_e(\infty)$, is set equal to the calculated average downstream ion beam density. As a result, downstream potentials are determined self consistently; there is no need to assume a neutralization plane. These codes include focusing effects and the fact that the aperture dimensions are usually significantly larger than the gap size such that the electric fields are reduced from the ideal maximum.

The potential distributions are calculated using an optimized pre-conditioned least-square conjugate gradient sparse matrix solver. Results for a given upstream plasma number density, n, are found by starting from zero density and iterating. At each iteration, i, a fraction, α, of the desired discharge chamber ion density is blended into the code:

$$n^0 = 0$$
$$n^{i+1} = \left(1-\alpha\right)n^i + \alpha n. \tag{5.3-3}$$

The density that the code uses asymptotically approaches the final density:

$$n - n^i = n\left(1-\alpha\right)^i. \tag{5.3-4}$$

If α is sufficiently small, approximate results for all upstream densities less then n can be obtained in a single run:

$$n^i = \left[1-\left(1-\alpha\right)^i\right]n. \tag{5.3-5}$$

By saving the intermediate results, only a single run is needed to estimate the performance of an optics design over a wide range of discharge chamber densities. However, since the calculation is fully converged only at the final density, separate runs with different final densities may be necessary to obtain accurate results over the full range of discharge chamber ion densities. A typical CEX-2D calculation takes a few minutes on a personal computer. Ion optic assemblies designed using the CEX-2D code have met the predicted performance very closely [4], illustrating that grid design techniques are very mature.

The ion density in the beamlet is obtained in the codes by tracking representative ion trajectories and accounting for charge exchange collisions that alter the ion energy. Ions enter the computational region from the upstream boundary at the Bohm velocity, and their charge density is found by following their trajectories in a stationary electric field. This is in contrast to the time-dependent particle in cell (PIC) technique generally used in plasma physics simulations.

An example of ion trajectories calculated by CEX-2D is shown in Fig. 5-6, which shows the computational space with the dimensions given in meters used for three values of beam perveance for half a beamlet in a three-grid configuration. In this figure, ions from the discharge chamber enter from the left and are accelerated by the electric field between the screen and accel grids. The horizontal boundaries represent lines of symmetry such that an ion crossing at these boundaries has another ion coming in from outside the domain. Figure 5-6(a) shows an *over-perveance* condition representing a beamlet current too high for the applied voltage, or too low a voltage for the plasma density and ion current provided. In this case, ions directly impinge on the upstream face of the accel grid. This situation is considered to be the *perveance limit*, where
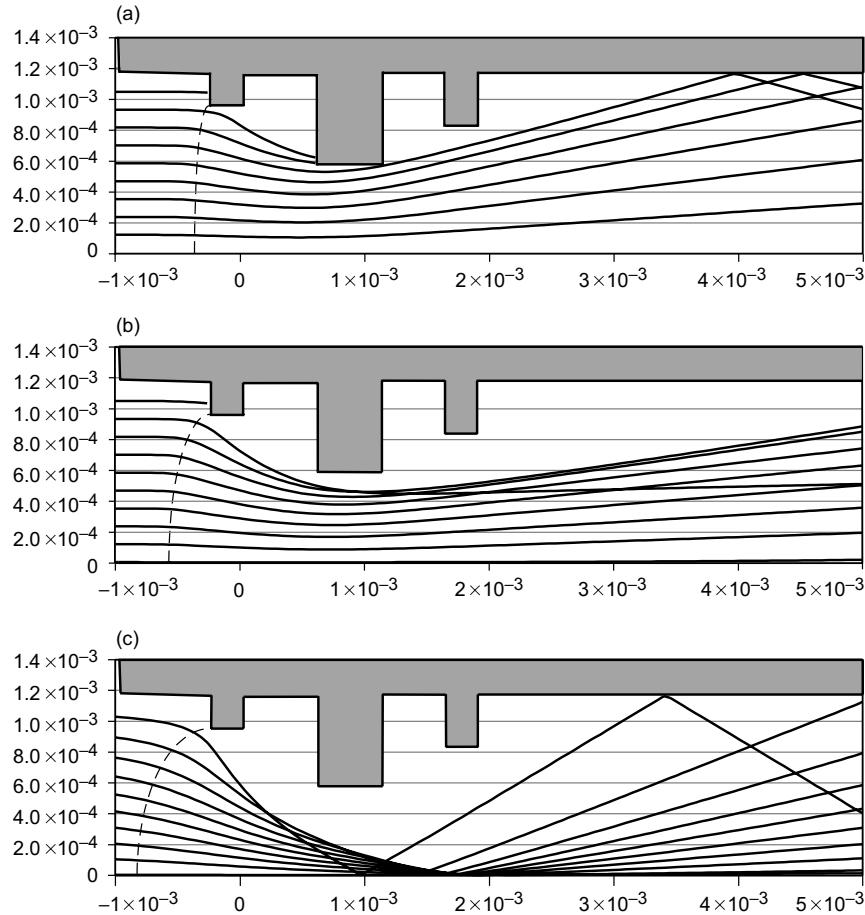
Fig. 5-6. Representative ion trajectories from a CEX2D calculation for three perveance conditions: (a) over-perveance with direct accel grid interception, (b) optimal perveance, and (c) under-perveance that can produce cross-over interception.

excessive ion current strikes the accel grid. Figure 5-6(b) shows a near-optimum perveance condition where the ions are well focused through the accel and decel grid apertures and do not directly intercept any downstream grid. Finally, Figure 5-6(c) shows an *under-perveance* condition where the ions are over focused and cross over in the accel gap. In this case, ions can directly intercept the accel grid and, eventually, the decel grid as the apertures wear open. Note that the length of the computational region shown must be long compared to its radius and is usually chosen so that neighboring beamlets will overlap.

A fraction of the ions from the plasma at the largest radii run directly into the screen grid, as seen in Fig. 5-6, and do not enter into the thrust beam. These ions represent the effect of the finite screen grid transparency that was so important in the discharge loss calculations in Chapter 4. For the near-optimal and under-perveance conditions, the screen grid transparency is greater than its geometric open area fraction, as mentioned above, because the self-consistent electric fields actually extract some of the ions at large radii that would have hit the screen grid instead of going into the screen aperture.

5.3.2   Perveance Limits

Figure 5-6 demonstrated that electrostatic accelerators produce focused ion trajectories when operated near a given design perveance and avoid grid interception or large beam divergence angles over a limited range of voltages and currents that are related by space charge considerations in the grid gap. In ion thrusters, operating sufficiently away from the perveance design of the grids results in beam interception on the downstream accel and (eventually) decel grids. Figure 5-7 shows an illustration of the accel grid current as a function of the current in a beamlet (a single aperture) for three different beam voltages. In this case, the optics were designed to run at about 2 kV and 0.8 mA of beamlet current, and the design demonstrates low grid interception over about ±50% of this current. As the beamlet current is increased, by raising the plasma density in the discharge chamber, the sheath thickness in the acceleration gap decreases, which flattens the sheath and causes the accel grid interception to increase. Eventually, the system becomes under-focused at the perveance limit where a large fraction of the beamlet is intercepted, as shown in Fig. 5-6(a). The accel grid current then increases rapidly with beamlet current due to the
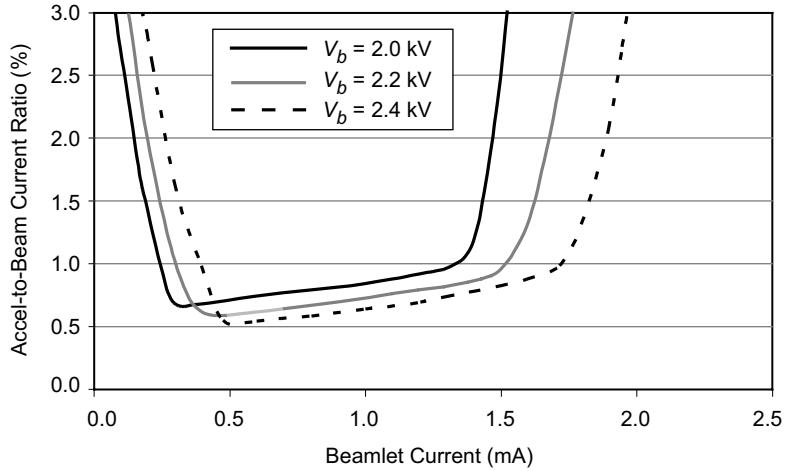

Fig. 5-7. Accel grid current-to-beam current ratio as a function of the beamlet current for three values of the beam voltage.

system running at too high a perveance. At low discharge chamber plasma densities, which produce low beamlet currents, the beam is over-focused and interception of the ions on the accel grid due to cross-over trajectories increases the accel grid current. The ion trajectories for this case are shown in Fig. 5-6(c).

At the nominal beam voltage of 2 kV, this system can be run from about 0.4 to 1.2 mA of beamlet current between the cross-over and perveance limits without producing excessive accel grid current. If the ion thruster has a current profile greater than about 3:1 peak to edge over the grid diameter (due to a poor plasma density uniformity), then grid interception will occur either in the center or at the edge of the beam. Since the grids are normally designed to deal with the high perveance condition at the peak current density near the axis, poor plasma profiles usually result in significant erosion of the edge holes due to cross-over interception. This will impact the life of the thruster and must be compensated by either changing the grid gap or screen aperture sizes as a function of the radius or modifying the plasma generator to produce more uniform profiles.

Increasing the beam voltage shifts the curves in Fig. 5-7 to higher beamlet currents. This is clear from the dependence in the Child–Langmuir equation (Eq. 5.3-2) where the current scales as $V^{3/2}$ if the sheath thickness and grid dimensions are held constant. In Fig. 5-7, the perveance-limited beamlet current, where direct grid interception occurs, increases as $V^{3/2}$ as the beam voltage is raised. Figure 5-7 also illustrates that, in situations where the thruster power must decrease, which is typical of deep space solar electric propulsion missions where the power available decreases as the spacecraft moves away from the Sun, the beam voltage and Isp of the thruster must eventually decrease as the current is reduced to avoid grid interception.

The voltage range available from a given accelerator design at a fixed (or nearly constant) beam current has limitations similar to the current dependence just discussed. However, the minimum voltage at a given current is of special interest in an ion thruster because this is related to the minimum Isp of the engine for a given thrust. The *perveance limit* of a thruster is usually defined relative to the rate at which the accel current increases as the beam voltage is decreased:

$$\text{Perveance limit} \equiv -0.02 \frac{I_A}{V_{\text{screen}}} \left[\text{mA/V}\right]. \tag{5.3-6}$$

This is related to the optics situation illustrated in Fig. 5-6(a), where the current at a given voltage is too high for the designed gap and aperture size and the under-focused beamlet starts to directly intercept accel grid. Figure 5-8 shows the behavior of the accel grid current for the NASA Solar Electric Propulsion
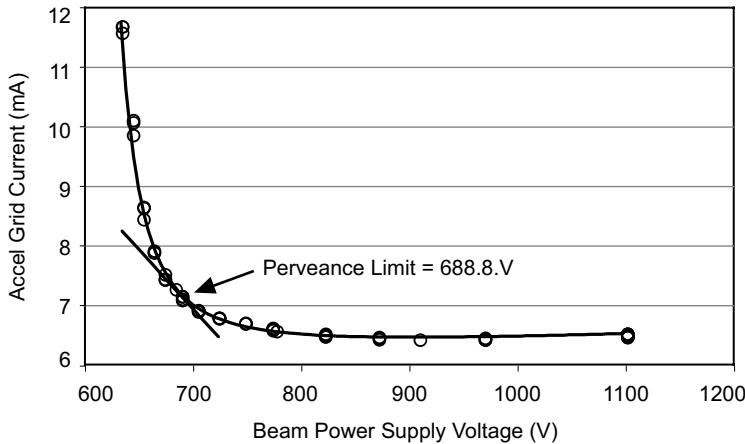
Fig. 5-8. Accel grid current versus the screen supply voltage for the NSTAR thruster at TH15 parameters, showing the perveance limit.

Technology Applications Readiness (NSTAR) engine operating at the full power parameters of TH15 but with the screen voltage decreasing. In this case, the perveance limit is found to be at 688.8 V, compared to the nominal 1100 V of the screen voltage at this throttle level. The perveance limit can also be defined by a given percentage increase in the accel current. However, the screen grid transparency usually decreases as the screen power supply voltage is decreased, which reduces the beam current and accel current during this measurement. The magnitude of the percentage increase in the accel current due to direct ion impingement then needs to be defined for the ion optics assembly.

5.3.3   Grid Expansion and Alignment

A significant issue in ion thrusters that utilize refractory metal grids is thermal expansion of the grids during thruster operation changing the acceleration gap dimension between the screen and accel grids. This will directly affect the ion trajectories and the perveance of the ion optics. Since the screen grid is heated by direct contact with the discharge plasma and is usually dished outwards and designed with a minimum thickness to increase the effective transparency, the screen grid expansion is usually larger than the accel grid and the gap tends to decrease as the thruster heats up. This shift from the *cold gap* to the *hot gap* causes the perveance of the optics to increase for convex grid curvature (grids domed outward from the thruster body) and changes the beamlet trajectories at the given operating point. In addition, for grids designed to hold the applied voltage across the cold gap, the hot gap may be so small that field emission and high voltage breakdown become problems. For ion thrusters with refractory metal grids designed with concave grid curvature (grids domed into the thruster

body), the screen grid expands away from the accel grid and the perveance decreases as the gap gets larger. In addition, concave grids have a smaller discharge chamber volume for a given thruster size, which adversely affects the discharge loss.

Ideally, the ion optics design would have sufficient margin to operate at full power over the range that the grid gap changes. This is possible for smaller thrusters and/or lower power levels where the grid deflection is a small fraction of cold gap. For thrusters with grid diameters greater than 15 to 20 cm operating at power levels in excess of 1 kW, it is often necessary to design the optics for the highest power case with the small hot gap, and to start the thruster in the diode mode (discharge only) or at lower beam powers to pre-heat the grids to avoid breakdown during thermal motion. This establishes the grid gap dimension within the range the optics can tolerate for high-power operation with minimal grid interception. It should be noted that grids fabricated from the various forms of carbon (graphite, carbon–carbon composite, or pyrolytic) have smaller or negligible thermal expansion than refractory metal grids and will have smaller grid gap changes. Ion optics sets that utilize grids made of two different materials have to deal with this issue of different thermal expansion coefficients and potentially larger grid gap changes.

Another significant grid issue is alignment of the grid apertures. The ion trajectories shown in Fig. 5-6 assumed perfect alignment of the screen and accel grid apertures, and the resultant trajectories are then axi-symmetric along the aperture centerline. Displacement of the accel grid aperture relative to the screen grid centerline causes an off-axis deflection of the ion trajectories, commonly called *beam steering*. The affect of aperture displacement on the beamlet steering has been investigated for many years in both ion sources and ion thrusters [22–25]. The beamlet is steered in the direction opposite to that of the aperture displacement due to the higher focusing electric field induced at the accel grid aperture edge. Studies of this effect in ion thruster grid geometries [24] show that small aperture displacements (≈10% of the screen aperture diameter) cause a deflection in the beamlet angle of up to about 5 degrees. This phenomenon can be used to compensate for the curvature of the grids to reduce the overall beam divergence, which is called *compensation*. However, the perveance of the aperture is reduced in this case, and interception of edge ions on the accel grid due to the non-uniform electric fields can be an issue. Mechanical misalignment of the grids due to manufacturing tolerances or thermal deformation can also produce aperture displacement and unintended beamlet steering. This problem has been identified as the cause of thrust vector variations observed as thrusters heat up [24]. For this reason, precise alignment of the grid apertures and grid support mechanisms that minimize non-uniform

thermal deformation are generally required to provide stable ion optics performance with minimal beam divergence.

5.4 Electron Backstreaming

Downstream of the accelerator grid, the ion beam is charge and current neutralized by electrons from the neutralizer hollow cathode. Since electrons are much more mobile than ions, a potential barrier is needed to stop neutralizer electrons from flowing back into the discharge chamber. In the absence of a potential barrier, the electron current would be several hundred times the ion current, wasting essentially all of the electrical power. The potential barrier is produced by the negatively biased accel grid. The minimum potential established by the accel grid prevents all but the highest energy electrons from traveling backwards from the beam plasma into the discharge chamber. The so-called "backstreaming" electron current is not only a parasitic power loss since these electrons do not add thrust, but it can damage the thruster by overheating the internal components of the discharge chamber such as the cathode.

The accel grid bias voltage required to limit the electron backstreaming current to a small value (typically <1% of the beam current) can be determined by evaluating Poisson's equation in the grid aperture in the presence of the beamlet ion current with 2-D computer codes. An example of such a calculation is shown in Fig. 5-9, where the potential between the electrodes and on the axis of the half-beamlet is shown. Note that the potential minimum in the center of the beamlet is only a small fraction of the applied accel grid voltage in this
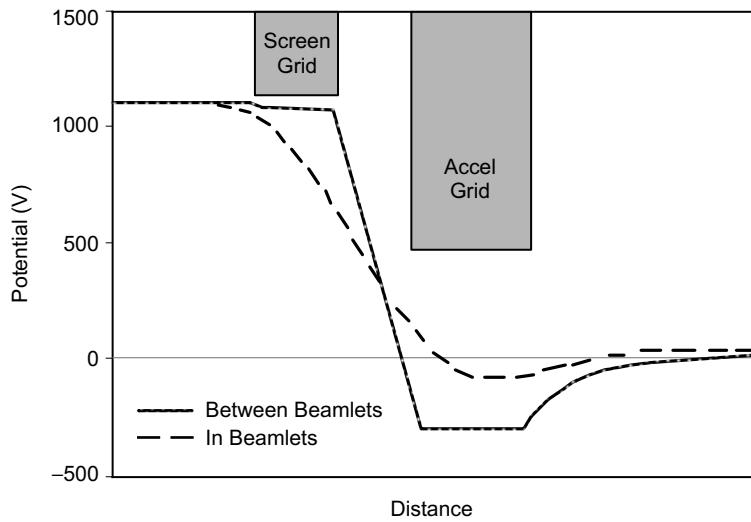

Fig. 5-9. Potentials on-axis in an individual beamlet and between the beamlets intersecting the grids.

example, which is due to the beam's space charge. The actual value of this minimum potential determines the margin to backstreaming, which should be set well above the value at which excessive backstreaming occurs.

Examining electron backstreaming in more detail shows that the minimum potential in the accel grid is determined by three factors: the electrostatic potential from the bias voltages applied to the different grids, the beamlet space charge in the accel grid aperture, and the required potential difference between the beam plasma and minimum voltage to reduce the backstreaming electron current to insignificant levels. Each of these factors can be evaluated analytically using simplifying approximations to help in understanding backstreaming physics.

As stated above, the backstreaming electron current results from the tail of the beam Maxwellian electron distribution overcoming the potential barrier established in the accel grid aperture. The current of electrons backstreaming into the thruster plasma is just the beam plasma random electron flux times the Boltzman factor for the potential difference between the beam plasma and the minimum potential in the accel grid region [26]:

$$I_{eb} = \frac{1}{4} ne \left(\frac{8kT_e}{\pi m} \right)^{1/2} e^{\frac{-(V_{bp} - V_m)}{T_e}} A_a , \qquad (5.4\text{-}1)$$

where I_{eb} is the electron backstreaming current, V_{bp} is the beam plasma potential, V_m is the minimum potential in the grid aperture, and A_a is the beamlet area in the grid aperture. The current of ions in the beamlet flowing through the grid aperture is

$$I_i = n_i e v_i A_a , \qquad (5.4\text{-}2)$$

and the ion velocity through the system is

$$v_i = \sqrt{\frac{2e\left(V_p - V_{bp}\right)}{M}} , \qquad (5.4\text{-}3)$$

where V_p is the plasma generator plasma potential at the sheath edge. Combining Eqs. (5.4-1) through (5.4-3), the minimum potential is

$$V_m = V_{bp} + T_e \ln \left[\frac{2I_{eb}}{I_i} \sqrt{\pi \frac{m}{M} \left(\frac{V_p - V_{bp}}{T_e} \right)} \right] . \qquad (5.4\text{-}4)$$

This equation describes the required potential difference between the beam potential and the minimum potential in the beamlet to produce a specified amount of electron backstreaming current relative to the beam current. Note that this equation is independent of the grid geometry because it deals solely with the potential difference between a given value of V_m (independent of how it is produced) and the beam-plasma potential. The required potential difference $(V_{bp} - V_m)$ between the beam plasma and the minimum voltage in the grids to produce a given ratio of backstreaming current to beam current is plotted from Eq. (5.4-4) in Fig. 5-10 for several values of the beam-plasma electron temperature in a thruster plume with a net accelerating voltage of $V_p - V_{bp} = 1500 \text{ V}$. For an electron temperature of 2 eV in the beam, which is consistent with values found in NSTAR thrusters plumes [27], a potential difference between the minimum potential in the beamlet and the beam plasma of only 12.5 V is required to reduce the backstreaming current to 1% of the beam current.

The actual minimum potential in the beamlet is determined by the grid geometry, the applied grid potentials, and the beam's space charge. The minimum potential in the two-grid arrangement shown in Fig. 5-5 was first found without considering space charge effects by an analytic solution to LaPlaces' equation by Spangenberg [28] for thin grids in vacuum tubes. Spangenberg's expression was simplified by Williams [26] and Kaufman [1] for most ion thruster grid configurations to
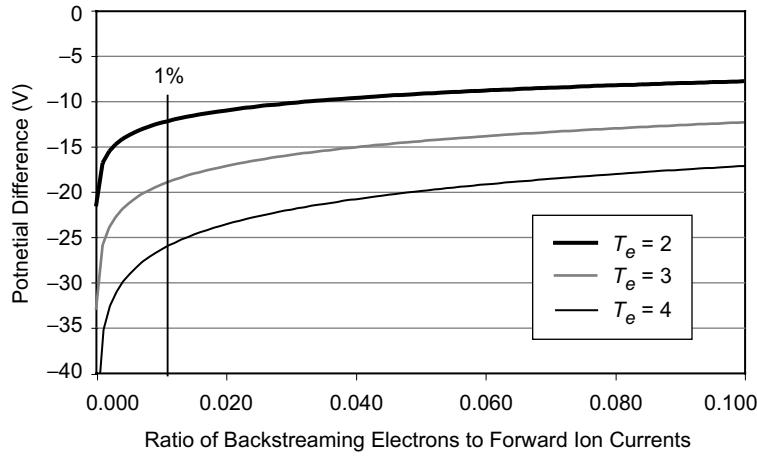
Fig. 5-10. Potential difference between the beam plasma and the beamlet potential minimum required to achieve a given electron backstreaming current-to-forward ion current ratio for several beam electron temperatures.

$$V_m^* = V_a + \frac{d_a(V_p - V_a)}{2\pi\ell_e}\left[1 - \frac{2t_a}{d_a}\tan^{-1}\left(\frac{d_a}{2t_a}\right)\right]e^{-t_a/d_a}, \tag{5.4-5}$$

where V_m^* indicates the minimum potential with the ion space charge neglected, V_a is the applied accel grid potential, the grid dimensional terms are defined in Fig. 5-5, and ℓ_e is given by Eq. (5.2-3). Equation (5.4-5) provides the dependence on the geometry of the grids, but is only useful if the beam space charge is negligible (very low current density beamlets).

The reduction in the magnitude of the minimum beam potential due to the presence of the ion space charge in the beamlet can be estimated [26] using the integral form of Gauss's law:

$$\oint_S \mathbf{E} \cdot d\mathbf{A} = \frac{1}{\varepsilon_o}\int_V \rho \, dV, \tag{5.4-6}$$

where $\mathbf{E}$ is the electric field, $d\mathbf{A}$ is the differential surface area element, ε_o is the permittivity of free space, and ρ is the ion charge density within the Gaussian surface which has a surface area S and encloses volume V. This equation is solved first in the beamlet and then in the charge-free space between the beamlet and the accel aperture inside diameter. Then, adding the two potentials together gives the total potential between the grid and the beamlet centerline.

Assume that the beamlet has a radius $d_b/2$ inside the accel grid aperture with a radius of $d_a/2$. Integration of the left-hand side of Eq. (5.4-6) over a cylindrical "Gaussian pillbox" aligned with the beamlet axis yields

$$\oint_S \mathbf{E} \cdot d\mathbf{A} = \int_0^{2\pi}\int_0^{r_a} E_r \, rd\theta \, dz = E_r \, 2\,\pi\,r\,z, \tag{5.4-7}$$

where it has been assumed that E_r is constant in the axial direction over a distance z. If it is also assumed that the ion charge density is uniform in the volume of the pillbox, the right-hand side of Eq. (5.4-6) can also be integrated to obtain

$$\frac{1}{\varepsilon_o}\int_V \rho \, dV = \frac{1}{\varepsilon_o}\int_V \rho \, r \, dr \, d\theta \, dz = \frac{\rho}{\varepsilon_o}\pi\,r^2\,z. \tag{5.4-8}$$

Equating Eqs. (5.4-7) and (5.4-8), an expression for the radial electric field in the beamlet (E_{r1}) from the accel hole centerline to the outer edge of the beamlet is obtained:

$$E_{r1} = \frac{\rho\, r}{2\, \varepsilon_o}, \qquad \left(0 < r < \frac{d_b}{2}\right). \tag{5.4-9}$$

From the edge of the beam to the wall, Gauss's law is again used, but in this case the entire beam charge is enclosed in the Gaussian surface. The radial electric field in this "vacuum region" outside the beamlet (E_{r2}) is then found in a similar manner to be

$$E_{r2} = \frac{\rho d_a^2}{8\varepsilon_o r}, \qquad \left(\frac{d_b}{2} < r < \frac{d_a}{2}\right). \tag{5.4-10}$$

The voltage difference ΔV from the centerline to the accel grid barrel due to the ion space charge is obtained by integrating the electric field between these limits. Hence,

$$\Delta V = -\int_0^{d_b/2} E_{r1} dr - \int_{d_b/2}^{d_a/2} E_{r2} dr = -\int_0^{d_b/2} \frac{\rho r}{2\varepsilon_o} dr - \int_{d_b/2}^{d_a/2} \frac{\rho\, d_b^2}{8\, \varepsilon_o\, r} dr. \tag{5.4-11}$$

The total potential from the accel wall to the center of the beamlet due to ion space charge is then

$$\Delta V = \frac{\rho d_b^2}{8\varepsilon_o} \left[\ell n\left(\frac{d_a}{d_b}\right) + \frac{1}{2}\right]. \tag{5.4-12}$$

The beam current density in the accel aperture is the charge density times the beam velocity, so the ion charge density ρ is

$$\rho = \frac{4\, I_i}{\pi\, d_b^2\, v_i}, \tag{5.4-13}$$

where v_i is the ion velocity evaluated at the minimum potential point:

$$v_i = \sqrt{\frac{2e\left(V_p - V_m\right)}{M}}. \tag{5.4-14}$$

Substituting Eqs. (5.4-13) and (5.4-14) into Eq. (5.4-12) gives

$$\Delta V = \frac{I_i}{2\pi\varepsilon_o v_i}\left[\ell n\left(\frac{d_a}{d_b}\right) + \frac{1}{2}\right]. \tag{5.4-15}$$

Since scalar potentials can be added, the sum of Eqs. (5.4-15) and (5.4-5) gives the total of the potential minimum in the accel grid aperture.

$$V_m = V_a + \Delta V + \frac{d_a(V_{bp} - V_a)}{2\pi\ell_e}\left[1 - \frac{2t_a}{d_a}\tan^{-1}\left(\frac{d_a}{2t_a}\right)\right]e^{-t_a/d_a}. \tag{5.4-16}$$

To calculate the backstreaming current as a function of grid voltage, Eq. (5.4-16) must be equated to Eq. (5.4-4) and solved for the current:

$$\frac{I_{be}}{I_i} = \frac{e^{(V_a + \Delta V + (V_{bp} - V_a)C - V_{bp})/T_e}}{2\sqrt{\pi\dfrac{m}{M}\dfrac{(V_p - V_{bp})}{T_e}}}, \tag{5.4-17}$$

where the geometric term C is given by

$$C = \frac{d_a}{2\pi\ell_e}\left[1 - \frac{2t_a}{d_a}\tan^{-1}\left(\frac{d_a}{2t_a}\right)\right]e^{-t_a/d_a}. \tag{5.4-18}$$

In practice, the onset of backstreaming is determined by two techniques. One method is to monitor the increase in the screen power supply current as the magnitude of the accel grid voltage is decreased. Increases in the measured current are due to backstreaming electrons, and a 1% increase is defined as the minimum accel grid voltage to avoid backstreaming: the so-called *backstreaming limit*. For example, the power supply current from Eq. (5.4-17), normalized to the initial beam current, is plotted in Fig. 5-11 as a function of the accel grid voltage for the NSTAR ion optics [29] for the maximum power throttle point TH15 at the beginning of life (BOL). In this figure, the beam potential and electron temperature were assumed to be 12 V and 2 eV, respectively, consistent with measurements made on this thruster. The onset of backstreaming occurs at about –150 V on the accel grid, which is consistent with the data from tests of this engine [30,31].

A second method for determining the backstreaming limit is to monitor the ion production cost, which is the discharge power required to produce the ion beam current divided by the beam current. This is an effective method for use in

thrusters operating in the beam-current-regulated mode where the discharge power supply is controlled to fix the beam current. Backstreaming then appears as a decrease in the ion production cost. This method is shown in Fig. 5-12 for the experimental data taken from the NSTAR thruster at TH15. As the magnitude of the accel voltage is decreased, a 1% decrease in the ion production cost represents the defined onset of backstreaming. In this case, the backstreaming limit was determined to be about –148 V, consistent with the above analytical model.

Fig. 5-11. Normalized beam current versus applied accel grid voltage, showing the onset of electron backstreaming as the voltage is decreased.
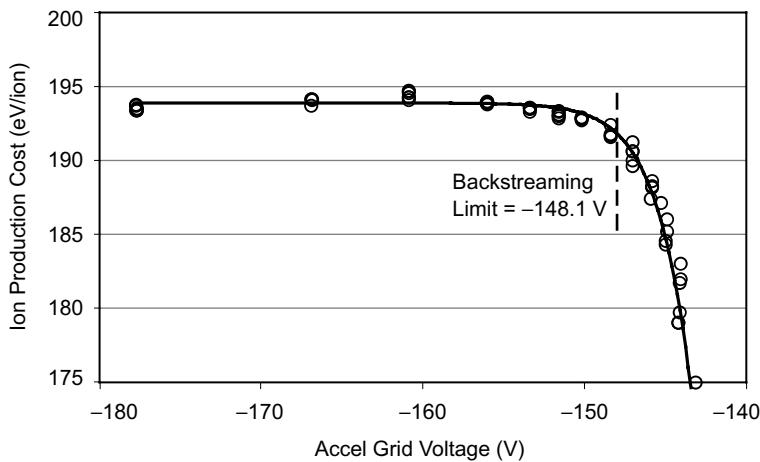

Fig. 5-12. Ion production cost for NSTAR TH15 versus applied accel grid voltage, showing the onset of electron backstreaming as the voltage is decreased.

Equations (5.4-17) and (5.4-18) show that the electron backstreaming is a function of the accel grid hole diameter. Increases in the accel hole diameter will reduce the penetration of the applied grid bias voltage to the center of the aperture and reduce the minimum potential on axis. This increases either the backstreaming current at a given voltage or the backstreaming limit at a given current. The effect of accel grid hole enlargement due to grid wear is illustrated in Fig. 5-13, where the grid voltage at which backstreaming started is plotted versus accel grid hole diameter for the NSTAR TH15 case measured during the extended life test (ELT) [31]. Larger grid-hole diameters required more negative biasing of the accel grid to avoid the onset of backstreaming.

Figure 5-13 also shows an interesting effect in that the shape of the grid hole is important. Early in life, the grid aperture diameter eroded due to sputtering, and the barrel diameter was adequately described by the minimum hole diameter observed optically during running of the test. However, as the test progressed, the erosion of the upstream aperture edge essentially stopped and the aperture was observed to be chamfered on the downstream portion. An effective grid diameter had to be calculated to take into account the non-uniform hole erosion in determining the backstreaming onset, shown on the right-hand side of Fig. 5-13. While the above analytical model accounts for grid diameter and thickness, additional terms would have to be added to account for this conical erosion shape. This situation is best handled by 2-D models that both determine the time-dependent shape of the grid hole and calculate the potential on axis appropriately.
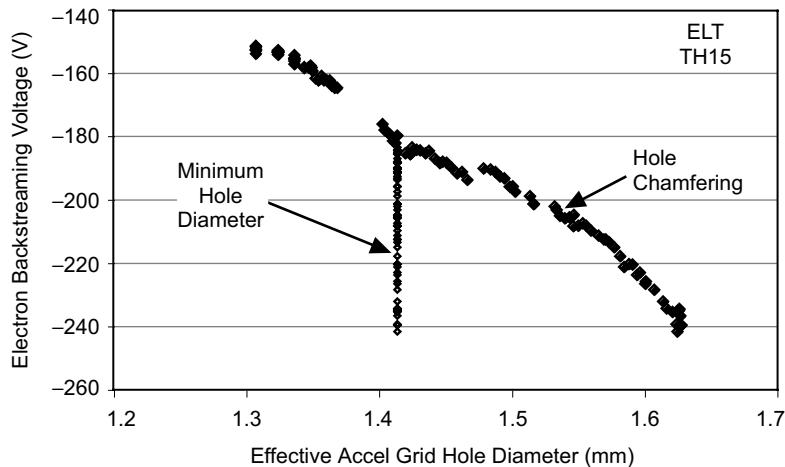

Fig. 5-13. Accel grid voltage at which electron backstreaming occurs in the NSTAR thruster at TH15 power level versus the effective accel grid aperture diameter.

It should be noted that while the analytical model described above illustrates the mechanisms involved in electron backstreaming and provides reasonable agreement with the experimental data shown, the results are very sensitive to the dimensions and beam parameters assumed in the calculation. This is largely because the potential minimum is the difference between two large numbers representing the contributions of the electrostatic fields and the space charge fields. Therefore, this backstreaming model actually provides only an estimate of the backstreaming voltage and current levels, which can easily be off 10% to 20%. The 2-D grid codes described above that solve Poisson's equation exactly provide more accurate calculations of the backstreaming limit.

Finally, electron backstreaming occurs first in the region of the highest beamlet current where the ion space charge is the highest in the ion optics assembly. Thrusters with non-uniform beam profiles, such as NSTAR with a flatness parameter (defined as average-to-peak current density) of about 0.5 and therefore a 2:1 peak-to-average current density profile [30], will tend to backstream primarily from the center beamlets. This localized backstreaming accelerates electrons on axis and can overheat components such as the cathode at the center-back of the thruster. Thrusters designed to have flat profiles, such as the Nuclear Electric Xenon Ion Thruster System (NEXIS), with a better than 0.9 flatness parameter [33], will tend not to backstream easily because of a lower peak ion current density for a given total beam current, and also, if backstreaming starts, it will be over a larger area that minimizes the localized heating issue in the discharge chamber.

5.5 High-Voltage Considerations

As shown in Section 5.3, the maximum thrust that can be produced by an ion thruster is a function of the electric field that can be sustained between the screen and accelerator grids:

$$T_{\max} = \frac{8}{9}\varepsilon_o \gamma\, T_s\, A_g\, \sqrt{R} E^2. \qquad (5.5\text{-}1)$$

From Eq. (5.5-1), the maximum space-charge-limited (sometimes called *perveance-limited*) thrust of the accelerator system is directly proportional to the intra-grid electric field squared. To produce compact ion thrusters with the highest possible thrust, it is necessary to maximize the electric field between the grids. The maximum thrust in ion engines is then limited primarily by the voltage hold-off capability of the grids.

The ability of the accelerator grids to hold off high voltage reliably and to withstand occasional breakdowns without significant damage or loss of voltage standoff capability is therefore of critical importance for ion thrusters. The high-voltage behavior of vacuum-compatible materials has been summarized in recent books on high-voltage engineering [34,35]. In plasma devices [36], electric fields of up to 40 kV/cm were found useful for refractory metal electrodes and of the order of 25 kV/cm for carbon materials. Degradation of the voltage hold-off due to surface damage incurred during breakdowns has been investigated for molybdenum and carbon electrodes [36] commonly used in ion thruster applications. The surfaces of these materials can be carefully prepared to withstand high electric fields required to produce the highest thrust density. However, sputter erosion over time and electrical breakdowns between grids cause some fraction of the stored energy in the power supply to be deposited on the grid surface. The formation of an arc at the cathode electrode (the accel grid) and the deposition of a significant amount of electron power from discharge into the anode electrode (the screen grid) can cause both the screen and accel grid surfaces to be modified and/or damaged. The breakdown events usually impact the subsequent voltage hold-off capability of the grid surfaces, which affects the long-term performance of the thruster.

5.5.1 Electrode Breakdown

The grids in ion thrusters have high voltages applied across small grid gaps, which can lead to high-voltage breakdown and unreliable thruster operation. High-voltage breakdown is usually described in terms of the electric field applied to the surface that causes an arc or discharge to start. Arc initiation is well correlated to the onset of field emission [37,38]. If sufficient field emission occurs due to excessive voltage or a modification to the surface that enhances field emission, the gap breaks down. Physical damage to arced surfaces during the breakdown is attributed to localized energy deposition on the electrode that causes melting or evaporation of the material. On the cathode surface (the accel grid), the energy is deposited primarily by ion bombardment from the arc plasma. On the anode surface (the screen grid), the energy is deposited from the plasma or electron stream that crosses the gap and results in localized surface heating and vaporization. The energy provided to the arc from the power supply is distributed between any series resistance in the electrical circuit, the voltage drop at the cathode surface, and the voltage drop in the plasma discharge and anode sheath. These voltage drops can be modeled using discrete series resistances in the energy balance of the system. Engineers often rate the possibility of a power supply damaging the electrodes by the amount of stored energy in the power supply. However, the amount of material removed from the surfaces and the lifetime of high-voltage electrodes is usually characterized [36] by the amount of current that passes through the arc. This "coulomb-transfer

rating" is related to the energy deposition in the electrodes in a simple manner. The power running in the arc is $P = IV_{\text{arc}}$, where I is the discharge current and V_{arc} is the voltage drop in the arc. Assuming that most of the voltage drop is in the cathode sheath, the energy E deposited by the arc on the cathode surface is

$$E = \int P\ dt = \int IV_{\text{arc}}\ dt\ . \tag{5.5-2}$$

The voltage drop of refractory metal and graphite arcs is nearly independent of the amount of current running in the arc up to several hundred amperes [39,40]. Therefore the arc voltage can be considered to be essentially a constant, and the energy deposited by the arc on the cathode is

$$E = V_{\text{arc}} \int I\ dt = V_{\text{arc}}\ Q\ , \tag{5.5-3}$$

where Q is the total charge transferred in the arc. The arc energy deposited on the cathode surface for a given electrode material is characterized by the total charge transferred by the thruster power supplies during the arc time and not just the stored energy in the power supply. Assuming that the arc remains lit during the entire time required to discharge the filter capacitor in the power supply, the total charge transferred through the arc is $Q = CV$, where C is the capacitance and V is the capacitor charging voltage. If the arc current falls below the minimum value to sustain the arc, called the "chopping current," and is prematurely extinguished, then the total charge transferred is reduced.

It should be emphasized that the amount of energy delivered to the cathode surface by the arc and the amount of damage to the surface incurred by material removal are independent of any series resistance in the circuit as long as the current is stable for the duration of the event (i.e., the current is above the chopping current). This means that simply adding a series resistor to one leg of the high-voltage power supply circuit or the accel grid circuit will not reduce the surface damage due to an arc unless the arc current drops to less than the chopping current. The only mechanism that reduces surface damage if the current is large compared to the chopping current is to limit the total charge transfer. This requires either reducing the power supply capacitance at a given voltage (which reduces the total stored energy) or actively shunting or opening the circuit to reduce the arc duration.

5.5.2   Molybdenum Electrodes

Molybdenum is a standard electrode material used in ion thrusters due to its low sputter erosion rate, ability to be chemically etched to form the aperture array, and good thermal and structural properties. The surface of the

molybdenum grid is often slightly texturized to retain sputtered material to avoid flaking of the sputter-deposited material [41]. The threshold voltage for the onset of field emission versus the gap spacing measured for molybdenum electrodes using a standard "plate-and-ball" test arrangement in a high vacuum facility [42] is shown in Fig. 5-14. The data show a classic power-law dependence of the threshold voltage with gap spacing for small gaps, which is sometimes called the "total voltage effect" [43]. While there are numerous possible mechanisms for the total-voltage effect, the increased gap reduces the surface electric field and the field emission current but increases the probability of an atom or particulate being ionized while traversing the gap. The ionized atom or particle is then accelerated into the cathode potential electrode and produces secondary electrons. If sufficient ionizations and secondary electrons are produced, the process cascades and the gap breaks down. Therefore, the voltage that can be held across a gap does not increase linearly with the gap dimension. This is equivalent to the Paschen breakdown [35] mechanism in gas-filled devices and is caused by the release of gases or particulates from the surfaces in vacuum gaps. After 10 arcs of 1 mC in charge transfer, the threshold voltage was measured again, and the threshold voltage was observed to increase for every gap tested, indicating that the surface was being conditioned. Improving voltage standoff of electrodes with a series of low coulomb-transfer arcs is common practice in the high-voltage industry and historically is often called "spot-knocking." This process removes small field emitters and tends to clean oxides and impurities off the surface without damaging the surface, which reduces the onset of field emission. Higher coulomb transfer arcs on molybdenum (10 and 20 mC) improve the voltage hold-off by cleaning larger areas of the surface and removing field emission sites. This effect will continue
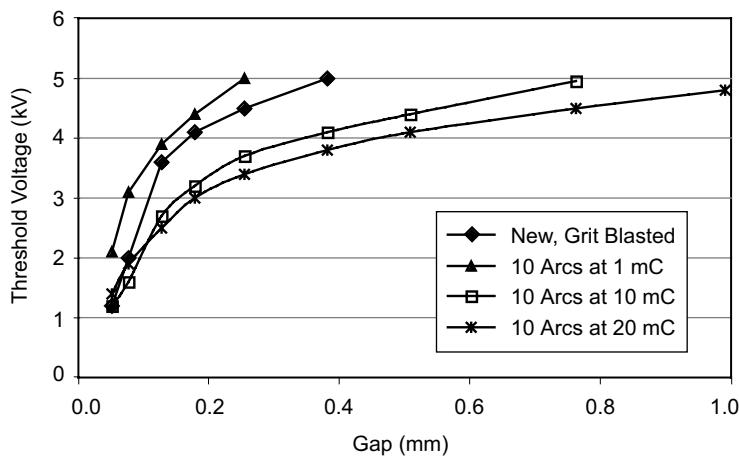

Fig. 5-14. Threshold voltage versus gap for molybdenum after 10 arcs of varying charge transfer (from [36]).

until the surface is well conditioned or the arc anchors in one spot and causes damage to the surface.

As the gap between the electrodes increases, the threshold voltage curves become more linear and the surface asymptotes to a constant threshold electric field. Figure 5-15 shows the threshold electric field for large gaps for a flat molybdenum surface texturized by grit blasting and actual texturized grid material with apertures chemically etched into the material. In this case, high coulomb transfer arcs tend to damage and degrade the voltage standoff of the grids. Scanning electron microscope photographs show localized damage to the edge of the beam apertures, resulting in more field emission sites. The molybdenum surfaces are initially capable of holding electric fields of well over 200 kV/cm, but the surface roughening to retain flakes and the aperture
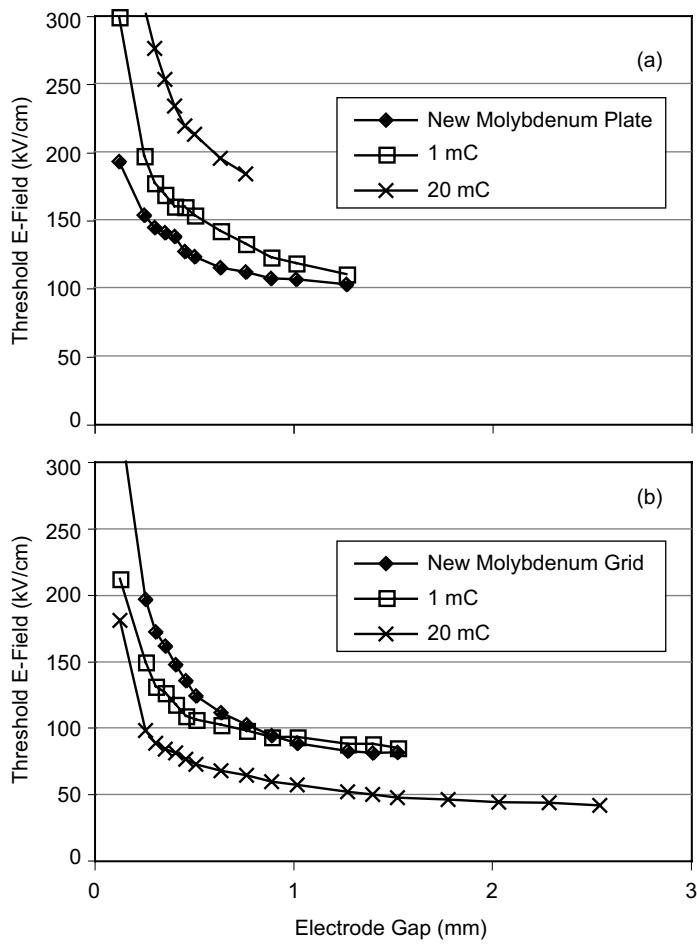

Fig. 5-15. Threshold electric field versus gap for (a) textured molybdenum plate and (b) textured grid material (from [36]).

edges associated with real grids cause the voltage hold-off to decrease. For molybdenum material with apertures, the resulting surface is susceptible to breakdown at electric fields of 40 to 50 kV/cm, which should be considered the maximum electric field for designing molybdenum grids.

5.5.3 Carbon–Carbon Composite Materials

Carbon is a desirable material for ion thruster grid electrodes because of its low sputtering yield under xenon ion bombardment [44] as compared with most refractory grid materials. However, the structural properties of graphite are usually insufficient for thin graphite grids of any reasonable size (greater than a 5- to 10-cm diameter) to survive launch vibrations. This problem can be solved by using carbon material with better structural properties, such as carbon–carbon composites and pyrolytic graphite. Grids made of these materials have demonstrated low erosion in life tests and flown successfully [45]. However, the more complex structures of these materials leads to lower thresholds for field emission and less voltage standoff for grids made of these materials.

Carbon–carbon composite material used for grid electrodes [46] is based on carbon fibers woven into a matrix with the fibers oriented in one or two dimensions. This material has enhanced strength and flexural modulus compared to pure graphite due to the carbon-fiber properties. The carbon-fiber weave is impregnated with a resin and built up to the desired shape by progressive laminate layers on a mold. The resulting material is usually densified and graphitized at high temperature, and may be further impregnated or over-coated with a thin chemical-vapor-deposition (CVD) carbon layer after this process to fill any voids or smooth the final surface. High-voltage breakdown tests were conducted with and without this final surface graphite coating.

The threshold voltage of the carbon–carbon composite samples is shown in Fig. 5-16, where the threshold for field emission is plotted as a function of the electrode gap for various levels of coulomb-transfer arcing. New material (without arcing) with a fresh CVD layer has a high threshold for field emission, and therefore holds voltage well. High coulomb-transfer arcs (>1 mC) tend to damage that surface and return it to the state of the material without the CVD over-layer. Higher coulomb-transfer arcs also tend to damage the surface. In fact, in this example, the 10-mC arcs resulted in damage to the opposite anode electrode, which evaporated and redeposited material back on the cathode-potential surface, improving its voltage hold-off capability. For this reason, the coulomb-transfer limit for carbon–carbon (CC) grids should be set to about 1 mC such that conditioning and no damage to either the screen or accel grid occurs during any breakdowns.

The threshold electric field for CC material with grid apertures is shown in Fig. 5-17 for new material and after a series of arcs. After the initial characterization with 10 arcs of 1 mC each, 10 arcs of 10 mC were delivered to the surface, which degraded the voltage standoff. However, the application of 4 sets of 10 arcs of only 1 mC re-conditioned the surface. The threshold electric field was found to asymptote to just below the same 40-kV/cm field at larger gap sizes observed for low coulomb-transfer arcs of flat material, suggesting that the aperture edges function in a similar manner as does material roughness.
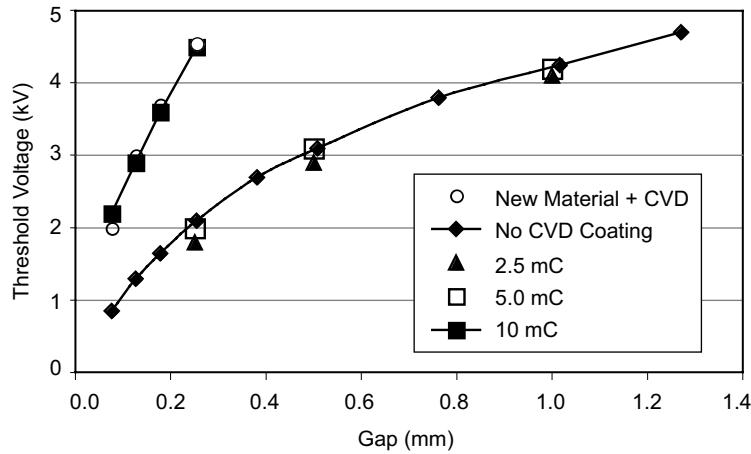
Fig. 5-16. Threshold voltage for carbon–carbon composite material after 10 arcs at various coulomb transfers (from [36]).
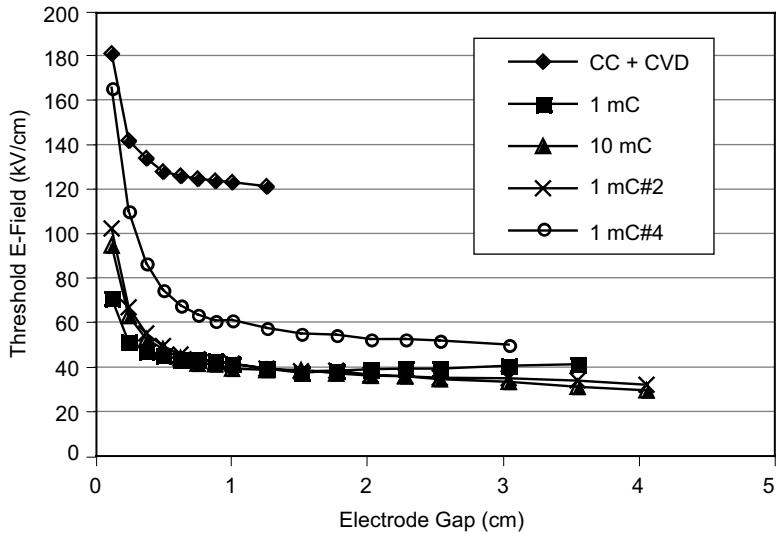
Fig. 5-17. Threshold electric field versus electrode gap for CC grid material with apertures (from [36]).

These results suggest that carbon–carbon composite grids can be designed for reliable high-voltage standoff utilizing a field emission threshold of about 35 kV/cm, even for large gaps and voltages in excess of 10 kV, provided that the coulomb transfer is limited by the power supply to less than about 1 mC. This 35-kV/cm field limit is the highest voltage stress that should be allowed, and conservative design practices suggest that a 50% margin (to ≈23 kV/cm) should be considered in designing these types of grids.

5.5.4 Pyrolytic Graphite

Pyrolytic graphite (PG) is also a candidate for accelerator grid electrodes in ion thrusters [47]. This material is configured with the carbon crystal planes parallel to the surface. Pyrolytic graphite is grown a layer at a time to near the desired shape on a mandrel and then finish machined to the final configuration. Flat test coupons were fabricated in this manner, but they featured small surface bumps and depressions that were residual from the growth process. Figure 5-18 shows the behavior of a PG grid sample that had apertures laser-machined into it and then the surface lightly grit blasted. The as-new PG material demonstrated threshold electric fields of 20 to 30 kV/cm for gaps of 1 mm or larger, which is lower than that found for the CC grid material. However, a series of ten 1-mC arcs tends to smooth and condition the surface and raise the threshold electric field to the order of 30 kV/cm. Higher coulomb arcs (up to about 10 mC) also improve the voltage standoff to about 40 kV/cm. The pyrolytic graphite is more susceptible to field emission and breakdown than the carbon–carbon material, but appears to tolerate higher coulomb-transfer arcs.
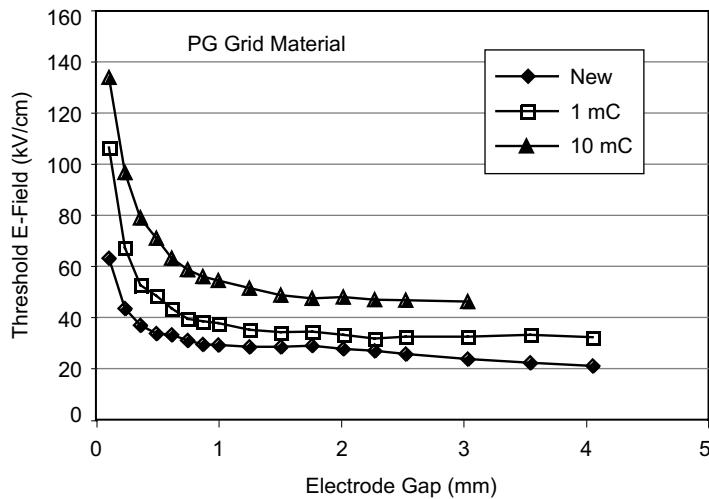

Fig. 5-18. Threshold electric field for pyrolytic graphite with grid apertures (from [36]).

5.5.5   Hold-off and Conditioning in Ion Thrusters

Tests have shown that the arc initiation voltage is directly related to the threshold voltage and electric field for field emission in Figs. 5-14 through 5-18 [36]. Arc initiation voltages tend to be less than 10% higher than the threshold values for field emission shown here. This is consistent with experimental observations that low levels of field emission and/or corona can be tolerated before full arc breakdown occurs, but arcing and recycling tend to increase once significant field emission starts. Molybdenum has been found to have a good tolerance for high coulomb-transfer arcs, and grids can be designed to reliably hold electric fields well in excess of 40 kV/cm. Carbon-based materials have more structure than the refractory metals and tend to form field emitters if excessive charge transfers are allowed. Nevertheless, grids utilizing carbon-based materials can be designed with electric fields in excess of 20 kV/cm if the coulomb transfer during breakdowns is limited to about 1 mC or less. Detailed investigations of the voltage hold-off and conditioning of carbon–carbon thruster grids were performed by Martinez [8], who documented the effect for larger area grid sets. Figure 5-19 shows their reduction in field emission from carbon–carbon grids plotted on a Fowler–Nordheim plot [43] for increasing numbers of 1-mC arcs. This work shows that even if the surface of carbon–carbon grids evolve field emitters over time due to erosion from ion bombardment, proper design of the power supply to limit the coulomb-transfer rate will result in reconditioning of the grid surfaces with every recycle event.
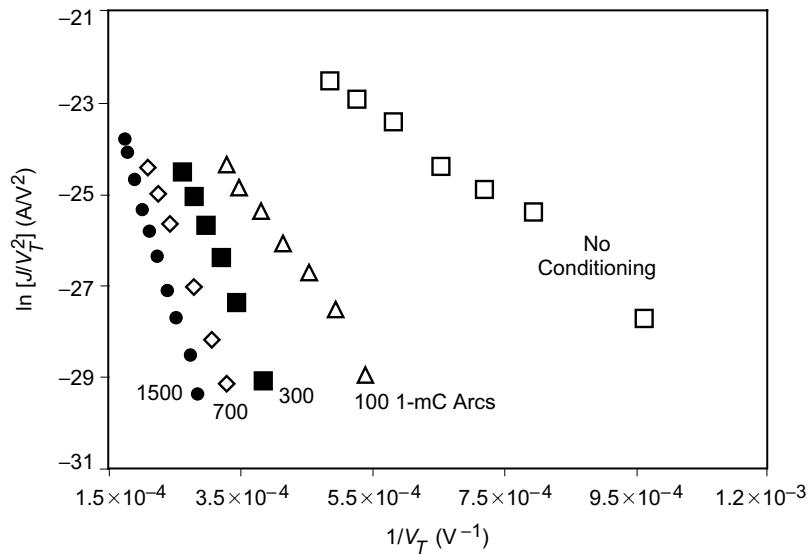

Fig. 5-19. Fowler–Nordheim plots of field emission, showing conditioning of carbon–carbon grids by increasing numbers of 1-mC arcs (from [8]).

5.6 Ion Accelerator Grid Life

The most important wear mechanism in modern ion thrusters is accelerator grid erosion. Even though properly designed optics attempt to make all of the ions extracted from the discharge chamber focus through the accelerator grid apertures, a current of secondary ions generated downstream of the discharge chamber impacts the accelerator grid. These secondary ions are generated by resonant charge exchange (CEX) between beam ions and neutral propellant gas escaping from the discharge chamber. The cross section for resonant charge exchange—that is, the transfer of an electron from a propellant atom to a beamlet ion—is very large: on the order of a hundred square angstroms [48]. This process results in a fast neutral atom in the beam and a slow thermal ion. These slow ions are attracted to the negatively charged accelerator grid, and most hit with sufficient energy to sputter material from the grid. Eventually the accelerator grid apertures become too large to prevent electron backstreaming or enough material is sputtered away that the grids fail structurally.

The erosion geometry is naturally divided into two regions. The first region, barrel erosion, is caused by ions generated between the screen grid aperture sheath and the downstream surface of the accelerator grid, as shown in Fig. 5-20. Charge exchange ions generated in this region impact the inside surface of the accelerator grid aperture, which results in enlargement of the aperture barrel. As the barrel diameter increases, the grid must be biased more and more negatively in order to establish the minimum potential required in the aperture to prevent neutralizer electrons from backstreaming into the discharge chamber. Thruster failure occurs when, at its maximum voltage, the accelerator grid power supply is unable to stop electron backstreaming.

The second region of grid erosion is caused by charge exchange ions generated downstream of the accelerator. Since the beamlets are long and thin, inside each beamlet the radial electric forces dominate and expel the slow, charge-exchange ions into the gaps between the beamlets. Charge exchange ions generated in the region before the beamlets merge to form a continuous ion density are then attracted back to the accelerator grid by its large negative potential. This is illustrated in Fig. 5-21. On impact, these ions sputter away material from the downstream surface of the accelerator grid. Sputter erosion by these backstreaming ions results in a hexagonal "pits-and-grooves" erosion pattern on the downstream grid surface, which can lead to structural failure of the grids if the erosion penetrates all the way through the grid. Erosion of the accel grid aperture edge by backstreaming ions can also effectively enlarge the accel grid aperture diameter, leading to the onset of electron backstreaming.
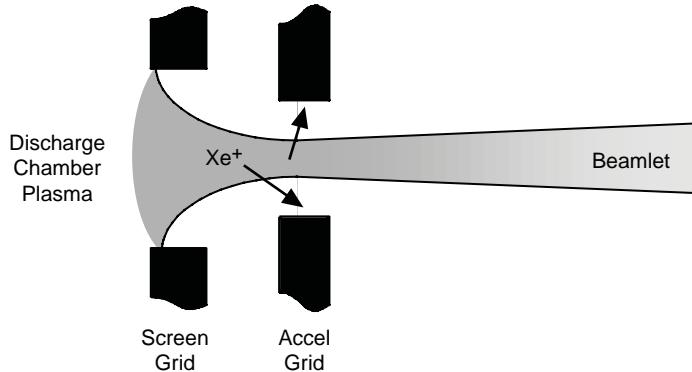
Fig. 5-20. Ions that cause barrel erosion are generated by charge exchange upstream and within the accelerator grid aperture.
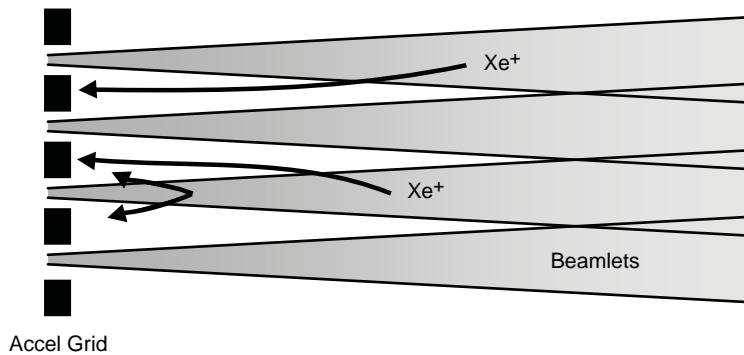

Fig. 5-21. Ions that cause pits and grooves erosion are generated between the downstream surface of the accel grid and where the beamlets overlap.

Erosion of the accelerator grid by charge exchange ion sputtering was the major life-limiting mechanism observed during the ELT of the NSTAR flight spare thruster [49] for operation at the highest power TH15 level. Photographs of center holes in the grid at the beginning and the end of the 30,000-hour test are shown in Fig. 5-22 where barrel-erosion enlargement of the aperture diameters is evident. Note that the triangle patterns where the webbing intersects in the end-of-test picture are locations where the erosion has completely penetrated the grid. The scanning electron microscope (SEM) photograph shown in Fig. 5-23 illustrates the deep erosion of the pits-and-grooves pattern and shows that full penetration of the grid had occurred when the test was stopped. Continued operation would have eventually resulted in structural failure of the grid, but this was not considered imminent at the end of the test.
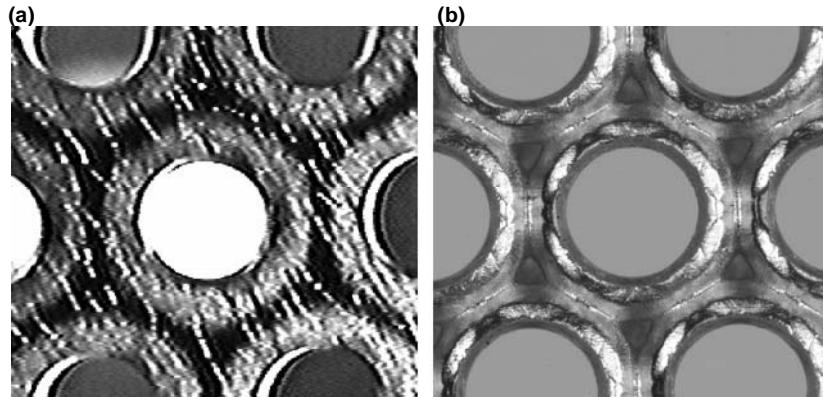
Fig. 5-22. NSTAR thruster accelerator grid at (a) 125 hours and (b) 30,352 hours.
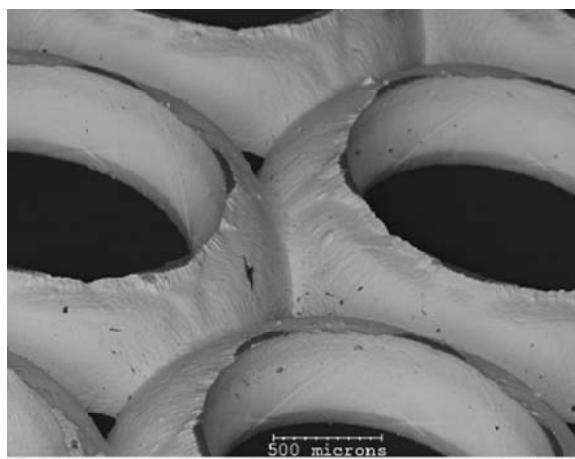

Fig. 5-23. SEM photograph shows that sputtering in the webbing between the holes had almost destroyed the structural integrity of the NSTAR grids.

5.6.1 Grid Models

As discussed above, the primary erosion mechanism of the accelerator grid is caused by sputtering from charge exchange ions. At the simplest level, all that is needed to predict erosion rates is to calculate the number of ions generated in the beamlets, find where they hit the grids, and then to determine the amount of material that they sputter. The total calculated charge exchange ion current accounts for nearly all of the measured accelerator grid current in a properly designed ion thruster (i.e., no direct interception of the beam current). The measured accelerator grid current in NASA's NSTAR thruster [30] ranged from

0.2% to 0.3% of the total beam current, which is shown in Fig. 5-24. Accel grid currents on the order of 1% or less of the beam current are standard in most ion thrusters.

Calculating the ion generation rate in the grid region due to charge exchange is relatively straightforward. The charge exchange currents generated by a single aperture's beamlet are given by

$$I_{CEX} = I_{Beamlet} \, n_o \, \sigma_{CEX} \, \ell_d, \qquad (5.6\text{-}1)$$

where ℓ_d is the effective collection length downstream of the accel grid from which ions flow back to the grid and n_o is the average neutral density along this length. The charge exchange cross section, σ_{CEX}, is well known and varies slowly with beam energy [48]. The average neutral density along the path length ℓ_d is estimated from the thruster propellant flow rate utilization fraction, which is the difference between the neutral atom flow rate and the beam ion current over the open area fraction of the accel grid. The neutral density is usually assumed to remain constant in the accel grid hole and decreases as the gas expands downstream of the grid surface. The neutral gas density is normally highest in holes near the edge of the grid and lower at the center where nearly all the gas has been "burned up" through ionization in the discharge chamber. The effective path length, ℓ_d, is a basic result of the ion optics calculations, and is essentially the distance downstream at which the beamlets have completely merged to form a beam plasma with a uniform potential across the beam diameter. An estimate of the effective path length is needed when setting up a grid erosion calculation to make certain that the
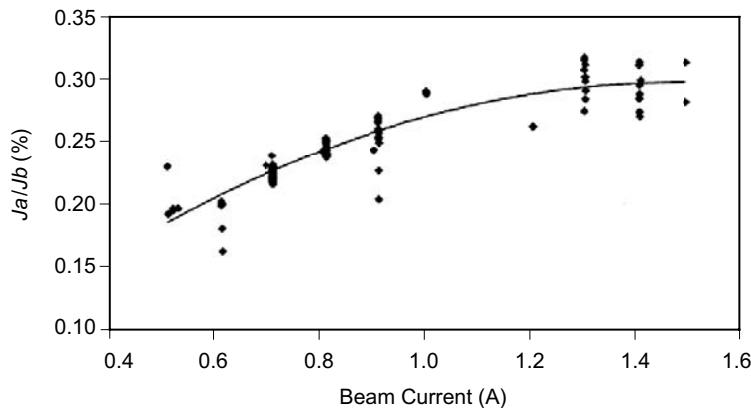

Fig. 5-24. Ratio of the accel grid current to the beam current as a function of the beam current in NSTAR, showing that the accel current is typically less than 1% of the beam current (from [30]).

computational region is long enough to include all the charge exchange ions that can return to the grid.

Using Eq. (5.6-1) and the current ratio from Fig. 5-24, an estimate can be made of the effective path length (ℓ_d) for the NSTAR thruster. If the measured accel grid current is all due to charge exchange (i.e., no direct interception), then Eq. (5.6-1) can be rewritten as

$$\ell_d = \frac{I_{\text{accel}}}{I_{\text{Beam}} \sigma_{\text{CEX}} n_o} .$$ (5.6-2)

Assuming the effective charge exchange path length is much longer than the gap between the screen and accelerator grids, the average neutral gas density can be estimated from the grid diameter, the flow of neutral gas out of the thruster, and the thruster beam current. The neutral gas density downstream of the grids close to the thruster is then

$$n_o = \frac{\Gamma_o}{v_o \, \pi \, r_{\text{grid}}^2} ,$$ (5.6-3)

where v_o is the neutral velocity, and Γ_o is the flux of unutilized propellant escaping from the discharge chamber. Using the parameters for the NSTAR at TH15 from [29], the total neutral flow into the thruster is 28 sccm. The thruster discharge chamber has a mass utilization efficiency of about 88%, so the neutral gas flow escaping the thruster is about 3.4 sccm, which corresponds to 1.5×10^{18} particles per second. Assuming the gas exits the thruster at about an operating temperature of 250°C, the neutral velocity $\bar{c}/2$ is about 110 m/s. The average neutral density from Eq. (5.6-3) is then about 2.3×10^{17} m^{-3}, and neutral density varies over the grid by more than a factor of two. Using the data in Fig. 5-24 extrapolated to the beam current of 1.76 A in TH15, and a charge exchange cross section of 5×10^{-19} m^2, the average effective path length from Eq. (5.6-2) becomes

$$\ell_d = \frac{(0.003)}{\left(5 \times 10^{-19}\right)\left(2.3 \times 10^{17}\right)} = 0.03 \, [\text{m}] .$$ (5.6-4)

The path length is more than an order of magnitude larger than the grid gap, consistent with our assumption. The very long path length compared with grid hole spacing means that the computational space in ion optics codes is very long (several centimeters), and so the computer codes must allow for the axial zone sizes to increase downstream of the grids.

5.6.2   Barrel Erosion

As was illustrated in Fig. 5-20, charge exchange ions generated between the screen grid and the upstream surface of the accel grid can impact the interior surface of the accel grid holes. These ions sputter away grid material, increasing the barrel radius. While computer codes, such as CEX-2D [4], are normally used to calculate the erosion rate, it is instructive to derive an analytical estimate. The following calculation is based upon published performance and erosion data for NASA's NSTAR thruster operating at its highest power TH15 level [29,50].

Assume that any ions generated downstream of the discharge chamber are not focused through the hole in the accelerator grid. For barrel erosion, the path length is taken as the sum of the grid gap and the accelerator grid thickness, which for NSTAR is about a millimeter. The upstream gas density is estimated by dividing the downstream density by the grid open area fraction, f_a, and the Clausing [51] factor, η_c, which reduces the gas transmission due to the finite thickness of the accel grid. The Clausing factor depends only on the aperture length-to-radius ratio. The neutral gas density is then

$$n_o = \frac{\Gamma_o}{v_o \, \pi \, r_{\text{grid}}^2} \, \frac{1}{f_a \eta_c} \; . \tag{5.6-5}$$

The neutral gas density in the accelerator grid apertures is higher than the gas density downstream of the accelerator grid, which was calculated using Eq. (5.6-2), due to the effects of the open area fraction and the Clausing factor. For an open area fraction of 0.24 and a Clausing factor of 0.6, the neutral density in the grid gap is about $9 \times 10^{18} \, \text{m}^{-3}$.

The number of grid apertures is approximately the grid open area divided by the area per aperture:

$$N_{\text{aperture}} \approx \frac{f_a \, \pi \, r_{\text{grid}}^2}{\pi \, r_{\text{aperture}}^2} \; . \tag{5.6-6}$$

The average aperture current is the total beam current divided by the number of apertures,

$$\overline{I}_{\text{aperture}} = \frac{I_b}{N_{\text{aperture}}} \; . \tag{5.6-7}$$

The maximum aperture current is obtained using the definition of beam flatness, which is given as

$$f_b \equiv \frac{\text{Average current density}}{\text{Peak current density}} = \frac{\overline{I}_{\text{aperture}}}{I_{\text{aperture}}^{\text{max}}}. \qquad (5.6\text{-}8)$$

The published value of NSTAR beam flatness from Polk [30] is 0.47. Using Eqs. (5.6-6), (5.6-7), and (5.6-8), the maximum current per aperture is 2.5×10^{-4} A. Charge exchange ions that can hit the accel grid are generated in between the screen grid exit and the accel grid exit. The distance d between the screen grid exit and the accel grid exit is about 1.12 mm [4]. The charge exchange ion current to the central aperture barrel is then

$$I_{\text{CEX}} = I_{\text{aperture}}^{\text{max}}\, n_o\, \sigma_{\text{CEX}}\, d = 1.4 \times 10^{-6}\,[\text{A}]. \qquad (5.6\text{-}9)$$

The CEX-2D computer code simulations [4] show that charge exchange ions hit the accelerator grid with about three-tenths of the beam potential. For NSTAR, the beam potential is 1100 V; thus, the average charge exchange ion energy is about 330 V. Using the curve fit in reference [4] for sputtering yield Y, the aperture atom sputter rate is obtained:

$$\dot{n}_{\text{sputter}} = \frac{I_{\text{CEX}}}{e} Y \approx 3.5 \times 10^{12}\ [\text{particles/s}]. \qquad (5.6\text{-}10)$$

This atom sputtering rate can be used to find an initial wall erosion rate by first calculating the volumetric erosion rate:

$$\dot{V}_{\text{aperture}} = \frac{\dot{n}_{\text{sputter}}}{\left(\dfrac{\rho_{Mo}}{M_{Mo}}\right)}, \qquad (5.6\text{-}11)$$

where the density of molybdenum is $\rho_{Mo} = 1.03 \times 10^4$ and the mass of molybdenum is $M_{Mo} = 95.94$ AMU $= 1.6 \times 10^{-25}$ kg. The volumetric erosion rate from Eq. (5.6-11) is then

$$\dot{V}_{\text{aperture}} = \frac{\dot{n}_{\text{sputter}}}{\left(\dfrac{\rho_{Mo}}{m_{Mo}}\right)} = \frac{3.5 \times 10^{12}}{\left(\dfrac{1.03 \times 10^4}{1.6 \times 10^{-25}}\right)} \approx 5.5 \times 10^{-17}\ [\text{m}^3/\text{s}]. \qquad (5.6\text{-}12)$$

Assuming the erosion rate is uniform throughout the barrel, the rate of increase of the aperture radius is just the volumetric erosion rate divided by the barrel area,

$$\dot{r}_{\text{aperture}} = \frac{\dot{V}_{\text{aperture}}}{2\,\pi\,r_a w_{\text{accel}}} \approx 3\times 10^{-11}\,[\text{m/s}]\,, \qquad (5.6\text{-}13)$$

where the accel grid aperture radius r_a is 0.582 mm and the accel grid thickness w_{accel} is a half-millimeter. For the 8200-hour NSTAR wear test results described by Polk [30], this corresponds to an increase in diameter of about 0.2 mm, roughly what was observed.

More accurate predictions of the accel grid barrel erosion rate are found using the 2D and 3D computer simulations [4]. However, the codes use the same basic technique as that shown here to determine the amount of material removed by the charge exchange sputtering. The better predictions result from more accurate calculations of the neutral density and ion current densities across the grid surfaces and through the grid apertures.

5.6.3   Pits-and-Grooves Erosion

Using three-dimensional ion optics codes, it is possible to reproduce the details of the pits-and-grooves geometry of accelerator grid downstream surface erosion. The JPL CEX-3D code was developed [17] to solve for potentials and ion trajectories in a two-grid ion optics system, and was later modified to include a third grid [52]. The computational domain, illustrated in Fig. 5-25, is a triangular wedge extending from the axis of a hole pair to the midpoint between two aperture pairs. The wedge angle of 30 degrees is chosen to give
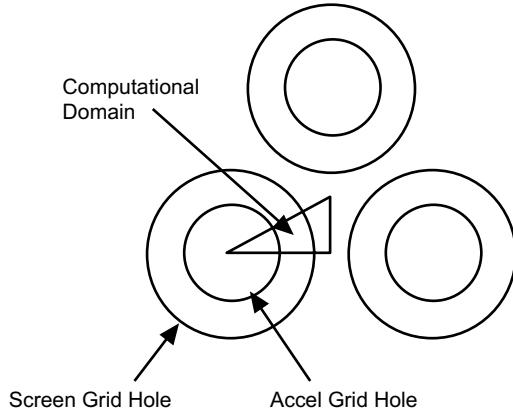

Fig. 5-25. Computational domain of the CEX-3D code (from [17]).

the smallest area that can be used to model the ion optics in order to minimize computational time. Similar triangles will cover each aperture pair by a combination of reflections and rotations. The computational domain extends from a few millimeters into the discharge chamber through the grids to a few centimeters downstream of the final grid.

In addition to tracking the beam-ion trajectories, the code calculates charge exchange ion production rates and charge exchange trajectories in three dimensions. Erosion of the accel grid barrel and downstream face is caused by these charge exchange ions. The location, kinetic energy, incidence angle, and current of each particle are recorded and used to compute the rate at which the grid material is removed. As shown above, charge exchange ions that strike the downstream surface of the accelerator grid can come from several centimeters downstream of the grid. Therefore, the computations domain is usually extended to 5-cm downstream of the final grid.

An example of the accel-grid downstream face erosion pattern predicted by CEX-3D is shown in Fig. 5-26. The triangular patches (the "pits"), where the grid webbing intersects, are shown in the photograph of the NSTAR ELT grid at the end of the test [49] and are predicted by the code in Fig. 5-26(a). In addition, the depth of the ring of erosion around the aperture ("the grooves") is also seen in Fig. 5-26(b) from the code predictions.

Accelerator grid pits-and-grooves erosion can be almost eliminated by the use of a third decelerator grid [44]. The Xenon Ion Propulsion System (XIPS®) thruster [53] is an example of an ion thruster that uses a three-grid ion optics system. As shown in Fig. 5-27, the third grid reduces from centimeters to

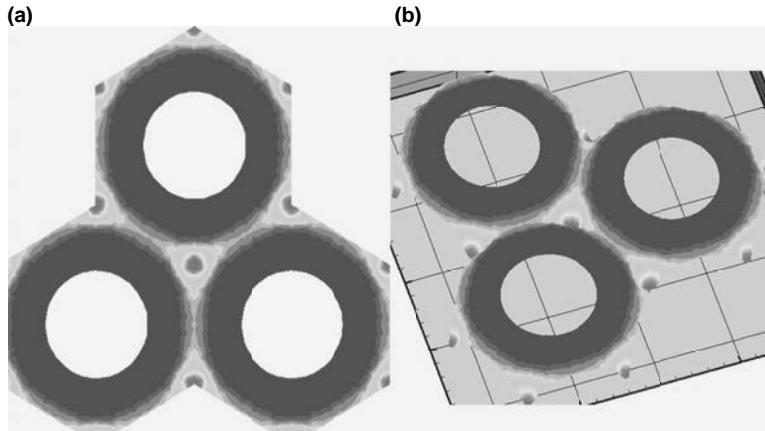(a)   (b)

Fig. 5-26. CEX-3D calculation of the pits-and-grooves erosion wear patterns that match the experimental patterns shown in (a) Fig. 5-22(a) and (b) 5-22(b).
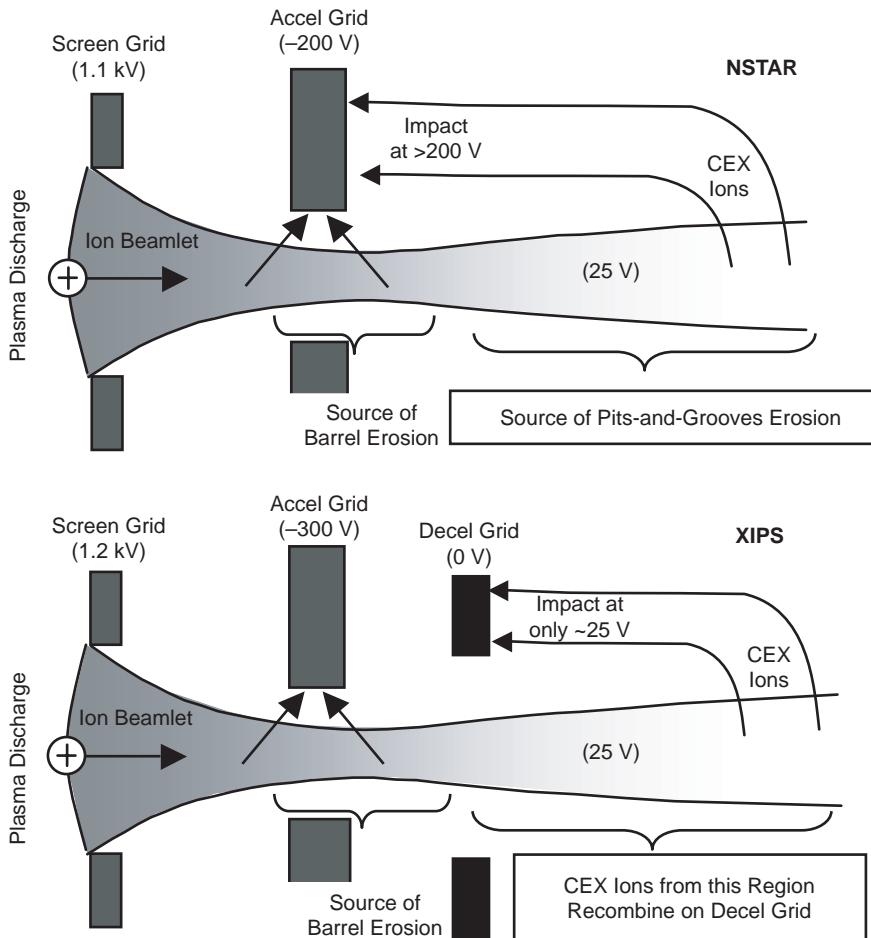
Fig. 5-27. Grid cross section comparing charge exchange generation in NSTAR, a two-grid system, with XIPS, a three-grid system.

millimeters the length of the region where charge exchange ions that can hit the accelerator grid are generated. This causes a dramatic reduction in the pits-and-grooves erosion between the two thrusters, shown in Fig. 5-28 as calculated using CEX-3D.

Although the three-dimensional code CEX-3D is used to predict erosion of the accelerator grid downstream surface, the simpler, two-dimensional CEX-2D code is typically used for accelerator grid aperture barrel erosion calculations because the apertures are cylindrical and the CEX2D code can produce these
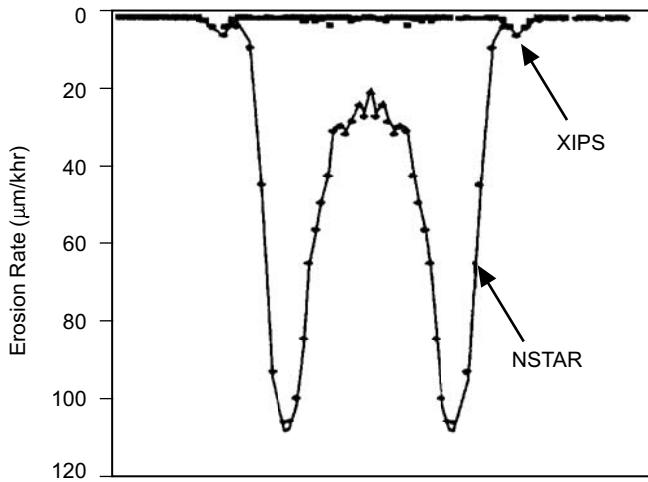
Fig. 5-28. CEX-3D results showing the XIPS third grid almost eliminates pits and grooves erosion evident in the NSTAR thruster (from [52]).

results more quickly. CEX-2D and CEX-3D use the same algorithms for the discharge chamber plasma and for beam ion trajectories. The codes have been benchmarked with each other, and for round beamlets that can be handled by CEX-2D, their results are within a few percent.

References

[1]   H. R. Kaufman, "Technology of Electron-Bombardment Ion Thrusters," in *Advances in Electronics and Electron Physics*, vol. 36, edited by L. Marton, New York: Academic Press, 1974.

[2]   A. T. Forrester, *Large Ion Beams*, New York: John Wiley and Sons, 1988.

[3]   G. R. Brewer, *Ion Propulsion Technology and Applications*, New York: Gordon and Breach, 1970.

[4]   J. R. Brophy, I. Katz, J. E. Polk, and J. R. Anderson, "Numerical Simulations of Ion Thruster Accelerator Grid Erosion," AIAA-2002-4261, 38th Joint Propulsion Conference, July 7–10, 2002.

[5]   V. J. Friedly and P. J. Wilbur, "High Current Hollow Cathode Phenomena," *Journal of Propulsion and Power*, vol. 8, no. 3, pp. 635–643, 1992.

[6]   I. Kameyama and P. J. Wilbur, "Measurement of Ions from High Current Hollow Cathodes Using Electrostatic Energy Analyzer," *Journal of Propulsion and Power*, vol. 16, no. 3, pp. 529–535, 2000.

[7]   P. J. Wilbur, J. R. Beattie, and J. Hyman, Jr., "An Approach to the Parametric Design of Ion Thrusters," *Journal of Propulsion and Power*, vol. 6, no. 5, pp. 575–583, 1990.

[8]   R. A. Martinez, J. D. Williams, and D. M. Goebel, "Electric Field Breakdown Properties of Materials Used in Ion Optics Systems," AIAA-2006-5004, 42nd Joint Propulsion Conference, Sacramento, California, July 10–13, 2006.

[9]   P. Wilbur, "Limits on High Specific Impulse Ion Thruster Operation," AIAA-2004-4106, 40th Joint Propulsion Conference, Fort Lauderdale, Florida, July 11–14, 2004.

[10] J. H. Whealton, R. W. McGaffey, and P. S. Meszaros, "A Finite Difference 3-D Poisson-Vlasov Algorithm for Ions Extracted from a Plasma," *Journal of Computational Physics*, vol. 63, pp. 20–32, 1986.

[11] Y. Arakawa and M. Nakano, "An Efficient Three Dimensional Optics Code for Ion Thruster Research," AIAA-96-3198, 32nd Joint Propulsion Conference, Lake Buena Vista, Florida, July 1–3, 1996.

[12] M. Nakano and Y. Arakawa, "Ion Thruster Lifetime Estimation and Modeling Using Computer Simulation," IEPC-99-145, 27th International Electric Propulsion Conference, Pasadena, California, October 15–19, 2001.

[13] Y. Nakayama and P. Wilbur, "Numerical Simulation of High Specific Impulse Ion Thruster Optics," IEPC-01-099, 27th International Electric Propulsion Conference, Pasadena, California, October 15–19, 2001.

[14] I. Boyd and M. Crofton, "Grid Erosion Analysis of the T5 Ion Thruster," AIAA-2001-3781, 37th Joint Propulsion Conference, Salt Lake City, Utah, July 8–11, 2001.

[15] Y. Okawa, H. Takegahara, and T. Tachibana "Numerical Analysis of Ion Beam Extraction Phenomena in an Ion Thruster," IEPC-01-097, 27th International Electric Propulsion Conference, Pasadena, California, October 15–19, 2001.

[16] J. Wang, J. E. Polk, J. R. Brophy, and I. Katz, "Three-Dimensional Particle Simulations of NSTAR Ion Optics," IEPC-01-085, 27th International Electric Propulsion Conference, Pasadena, California, October 15–19, 2001.

[17] J. J. Anderson, I. Katz, and D. Goebel, "Numerical Simulation of Two-Grid Ion Optics Using a 3D Code," AIAA-2004-3782, 40th Joint Propulsion Conference, Ft. Lauderdale, Florida, July 11–14, 2004.

[18] Ian Brown, *The Physics and Technology of Ion Sources*, New York: John Wiley and Sons, 1989.

[19] Y. Nakayama and P. J. Wilbur, "Numerical Simulations of Ion Beam Optics for Many-grid Systems," *Journal of Propulsion and Power*, vol. 19, no. 4, pp. 607–613, 2003.

[20] J. Kim, J. H. Wealton, and G. Shilling, "A Study of Two-stage Ion Beam Optics," *Journal of Applied Physics*, vol. 49, no. 2, pp. 517–524, 1978.

[21] C. Farnell, "Performance and Life Simulation of Ion Thruster Optics," Ph.D. Dissertation, Colorado State University, Fort Collins, Colorado, 2007.

[22] L. D. Stewart, J. Kim, and S. Matsuda, "Beam Focusing by Aperture Displacement in Multiampere Ion Sources," *Review of Scientific Instruments*, vol. 46, pp. 1193–1196, 1975.

[23] J. H. Whealton, "Linear Optics Theory of Ion Beamlet Steering," *Review of Scientific Instruments*, vol. 48, pp. 1428–1429, 1977.

[24] M. Tarz, E. Hartmann, R. Deltschew, and H. Neumann, "Effects of Aperture Displacement in Broad-Beam Ion Extraction Systems," *Review of Scientific Instruments*, vol. 73, no. 2, pp. 928–930, 2002.

[25] Y. Okawa, Y. Hayakawa, and S. Kitamura, "Experiments on Ion Beam Deflection Using Ion Optics with Slit Apertures," *Japanese Journal of Applied Physics*, vol. 43, no. 3, pp. 1136–1143, 2004.

[26] J. D. Williams, D. M. Goebel, and P. J. Wilbur, "Analytical Model of Electron Backstreaming for Ion Thrusters," AIAA-2003-4560, 39th Joint Propulsion Conference, Huntsville, Alabama, July 20–23, 2003.

[27] V. A. Davis, I. Katz, M. J. Mandell, D. E. Brinza, M. D. Henry, and D. T. Young, "Ion Engine Generated Charge Exchange Environment: Comparison between NSTAR Flight data and Numerical Simulations," AIAA-2001-0970, 39th Aerospace Sciences Meeting, Reno, Nevada, January 8–11, 2001.

[28] K. R. Spangenberg, *Vacuum Tubes*, New York: McGraw-Hill, p. 348, 1948.

[29] J. R. Brophy "NASA's Deep Space 1 Ion Engine," *Review of Scientific Instruments*, vol. 73 pp. 1071–1078, 2002.

[30] J. Polk, J. R. Anderson, J. R. Brophy, V. K. Rawlin, M. J. Patterson, J. Sovey, and J. Hamley "An Overview of the Results from an 8200 Hour Wear Test of the NSTAR Ion Thruster," AIAA Paper 99-2446, 35th Joint Propulsion Conference, Los Angeles, California, June 20–24, 1999.

[31] A. Sengupta, J. R. Brophy, and K. D. Goodfellow, "Status of the Extended Life Test of the Deep Space 1 Flight Spare Ion Engine After 30,352 Hours of Operation," AIAA-2003-4558, 39th Joint Propulsion Conference, Huntsville, Alabama, July 20–23, 2003.

[32] A. Sengupta, "Experimental Investigation of Discharge Plasma Magnetic Confinement in an NSTAR Ion Thruster," AIAA-2005-4069, 41st Joint Propulsion Conference, Tucson, Arizona, July 10–13, 2005.

[33] J. E. Polk, D. M. Goebel, I. Katz, J. S. Snyder, A. C. Schneider, L. Johnson, and A. Sengupta, "Performance and Wear Test Results for a 20-kW Class Ion Engine with Carbon-Carbon Grids," AIAA-2005-4393, 41st Joint Propulsion Conference, Tucson, Arizona, July 10–13, 2005.

[34] E. Kuffel and W. S. Zaengl, *High Voltage Engineering Fundamentals*, Oxford, England: Pergamon Press, 1984.

[35] W. H. Kohl, *Handbook of Materials and Techniques for Vacuum Devices*, New York: Reinhold Publishing Corporation, 1967.

[36] D. M. Goebel and A. C. Schneider, "High Voltage Breakdown and Conditioning of Carbon and Molybdenum Electrodes," *IEEE Transactions on Plasma Science*, vol. 33, issue 4, pp. 1136–1148, 2005.

[37] P. A. Chatterton, "Theoretical Study of the Vacuum Breakdown Initiated by Field Emission," *Proceedings of the Physics Society*, vol. 88, pp. 231–243, 1966.

[38] F. R. Schwirzke, "Vacuum Breakdown on Metal Surfaces," *IEEE Transactions on Plasma Science*, vol. 19, pp. 690–696, 1991.

[39] W. D. Davis and H. C. Miller, "Analysis of the Electrode Products Emitted by dc Arcs in a Vacuum Ambient," *Journal of Applied Physics*, vol. 40, pp. 2212–2221, 1969.

[40] A. Anders, B. Yotsombat, and R. Binder, "Correlation Between Cathode Properties, Burning Voltage, and Plasma Parameters of Vacuum Arcs," *Journal of Applied Physics*, vol. 89, pp. 7764–7771, 2001.

[41] J. S. Sovey, J. A. Dever, and J. L. Power, "Retention of Sputtered Molybdenum on Ion Engine Discharge Chamber Surfaces," IEPC-01-86, 27th International Electric Propulsion Conference, Pasadena, California, October 15–19, 2001.

[42] D. M. Goebel, "High Voltage Breakdown Limits of Molybdenum and Carbon-based Grids for Ion Thrusters," AIAA-2005-4257, 41st Joint Propulsion Conference, Tucson, Arizona, July 10–13, 2005.

[43] M. J. Druyvesteyn and F. M. Penning, "The Mechanism of Electrical Discharge in Gases," *Reviews of Modern Physics*, vol. 12, pp. 87–174, 1940.

[44] R. Doerner, D. White, and D. M. Goebel, "Sputtering Yield Measurements during Low Energy Xenon Plasma Bombardment," *Journal of Applied Physics*, vol. 93, no. 9, pp. 5816–5823, 2003.

[45] H. Kuninaka, I. Funaki, K. Nishiyama, Y. Shimizu, and K. Toki, "Results of 18,000 hour Endurance Test of Microwave Discharge Ion Thruster Engineering Model," AIAA-2000-3276, 36th Joint Propulsion Conference, Huntsville, Alabama, July 16–19, 2000.

[46] J. S. Snyder and J. R. Brophy, "Performance Characterization and Vibration Testing of 30-cm Carbon-Carbon Ion Optics," AIAA-2004-3959, 40th Joint Propulsion Conference, Ft. Lauderdale, Florida, July 11–14, 2004.

[47] M. De Pano, S. Hart, A. Hanna, and A. Schneider, "Fabrication and Vibration Results of 30-cm Pyrolytic Graphite Ion Optics," AIAA-2004-3615, 40th Joint Propulsion Conference and Exhibit, Fort Lauderdale, Florida, July 11–14, 2004.

[48] J. S. Miller, S. H. Pullins, D. J. Levandier, Y. Chiu, and R. A. Dressler, "Xenon Charge Exchange Cross Sections for Electrostatic Thruster Models," *Journal of Applied Physics*, vol. 91, no. 3, pp. 984–991, 2002.

[49] A. Sengupta, J. R. Brophy, J. R. Anderson, C. Garner, K. deGroh, T. Karniotis, and B. Banks, "An Overview of the Results from the 30,000 Hour Life Test of the Deep Space 1 Flight Spare Ion Engine," AIAA-2004-3608, 40th Joint Propulsion Conference, Fort Lauderdale, Florida, July 11–14, 2004.

[50] J. E. Polk, R. Y. Kakuda, J. R. Anderson, J. R. Brophy, V. K. Rawlin, M. J. Patterson, J. Sovey, and J. Hamley, "Performance of the NSTAR Ion Propulsion System on the Deep Space One Mission," AIAA-2001-965, 39th Aerospace Sciences Meeting and Exhibit, Reno, Nevada, January 8–11, 2001.

[51] P. Clausing, "The Flow of Highly Rarefied Gases Through Tubes of Arbitrary Length," *Journal of Vacuum Science and Technology*, vol. 8, pp. 636–646, 1971.

[52] R. Wirz and I. Katz, "XIPS Ion Thruster Grid Erosion Predictions for Deep Space Missions," 30th International Electric Propulsion Conference, Florence, Italy, September 17–20, 2007.

[53] J. R. Beattie, J. N. Matossian, and R. R. Robson, "Status of Xenon Ion Propulsion Technology," *Journal of Propulsion and Power*, vol. 6, no. 2, pp. 145–150, 1990.

Homework Problems

1. For an ion accelerator that is described by the Child–Langmuir law, derive the dependence of the minimum Isp on the beam voltage for a given thrust level.

2. A 1-kV ion accelerator has a grid spacing of 1 mm and a screen aperture diameter of 1 mm.

    a. What is the space-charge-limited beamlet current density for Xe^+ assuming a very thin screen grid and a planar sheath?

    b. If the screen grid is 0.25 mm thick, what is the maximum beamlet current density for a non-planar sheath? How does this compare to the classic planar Child–Langmuir result?

3. An ion thruster with a grid diameter of 20 cm has a beam current density that varies with the radius as kr^2, where k is a constant.

    a. If the peak current density on axis is J_p and the current density at the edge of the grid is $J_p/10$, find the expression for $J(r)$.

    b. If the peak current density is 5 mA/cm^2, what is the total beam current?

    c. What is the flatness parameter?

    d. What is the percent reduction in the beam current compared to the case of a uniform beam current density of the peak value (the flatness is 1)?

4. An ion thruster has a beam plasma potential of 20 V and an electron temperature in the beam of 5 eV.

    a. For a plasma potential at the screen grid sheath edge of 1000 V, what potential must be established in the accel grid aperture to keep the electron backstreaming current to 1% of the beam current?

    b. Neglecting space charge in the beamlet, what voltage must be applied to the accel grid to achieve the minimum potential in (a) for the case of a 3-mm screen grid diameter, 0.25-mm screen grid thickness, 2-mm accel grid diameter, and 0.5-mm accel grid thickness with a 1-mm grid gap?

    c. If the beamlet current is 0.2 mA and the beamlet has a diameter in the accel grid aperture of 1 mm, what must the accel grid voltage be to maintain the 1% backstreaming current specification?

5. One of the first ion thrusters to fly in space was a cesium surface ionization thruster where cesium ions were pulled from a hot surface by the electric field that also produced the beam. Model the thruster as a diode, with cesium ions at 7.5 mA/cm^2 coming from one surface and with the other electrode an accel grid with 80% transparency and a grid gap "d" from the ion source.

   a. Assuming 100% mass utilization efficiency, neglecting the angular divergence of the beam, and using a 200-V negative bias on the accel grid, what is the voltage, current, thruster diameter, and gap size required to produce 5 mN of thrust at an Isp of 3000 s?

   b. If the thruster has 95% mass utilization efficiency and a total angular divergence of the beam of 10 deg, how does that change the results of part (a)?

   c. If it takes 100 W of power to heating the cesium ion-emitting surface to the required surface temperature of about 1350 K, what is the total efficiency of the thruster, using the parameters from part (b)?